Master of Science in Energy and Nuclear Engineering
Politecnico di Torino - Department of Energy (DENERG)
Academic Year 2018-2019

Master of Science in Power and Nuclear Engineering

Atomistic study of radiation damage in advanced SiC grades

Academic Supervisor

Prof. **ZUCCHETTI** Massimo [a]

Company Supervisor

BONNY Giovanni, PhD [b]

Student

Firma del candidato
Buongiorno Ludovica (s240378)

July 2019

[a] Politecnico di Torino
[b] Universiteit Ghent, SCK•CEN

Acknowledgements

This work is the final step of my study career, which allowed me to be part of an exciting Erasmus+ Degree Program between Politecnico di Torino and SCK•CEN under the supervision of the University of Liège, which gave me the possibility to achieve the ambitious title of Nuclear Engineer recognized by ENEN society and all Europe. All the hurdles and the difficult moments I faced in these years would have been so hard without the help of some people that I want to acknowledge.

I want to thank my promoter in Politecnico di Torino, Massimo Zucchetti, for the encouragement and trust he gave me in these years as his student. It was an honour to have you as a professor and promoter for both the Bachelor and Master thesis.
I would like to thank my mentor and supervisor Giovanni Bonny, who followed me from the beginning of this master thesis project until the end.
He gave me strength and trust even if I didn't have the proper basis in computational molecular dynamics, and he offered me academic material and guidance in any moment I really needed it which allowed me to complete all the tasks I was supposed to fulfill. I hope that this thesis can be a proper beginning for bigger projects related to ATF technologies for PWRs.

Second, all my acknowledgements go to my boyfriend and life partner Alexandro Fulco, who was and is probably the only one who really believes in me and my skills, who gave me a proper place to live, taking care of me when I didn't have enough resources to continue my projects. He stayed and stays near me in positive and negative situations, supporting me every single moment of the day, following me in my life projects and ambitions. We created a beautiful family together in these two years and I hope one day I can do as much as he did for me. I love you, my dear.

Last but not least, I thank my family, not always supportive in my decisions, but always present when I needed help. To my real friends, Ashkhen, Verino, Andrea and all the others, I want to say thank you for not having abandoned me even if I am far away from you, who often call me, text me and listen to me when I need support. I hope you can enjoy this proclamation day.

I want to dedicate a little space to my uncle who died in may this year. Dear Zio Beppe, I know you would have been happy to see me graduating. Life decided to take you away from us, but, even if I was not physically near you, I always acknowledged your love for me and my sister, and this thesis is partially dedicated to you.

To Alexandro, my dear

To my Uncle Beppe

Abstract

Nowdays, SiC/PyC fibers are taken into account for accident tolerant fuel cladding, coatings and even structural components. Presently, many international efforts are focused in the Horizon 2020 IL TROVATORE® project to investigate the radiation tolerance of these classes of materials. In the present thesis, we use atomistic methods to explore the damage production and accumulation in the SiC/PyC composite.
Classical molecular statics will be applied to characterize the interaction of point defects near radiation defects and defects inherent to the material. Classical molecular dynamics will be applied to study the effect of the SiC/PyC interface on the primary damage production in SiC. SiC damage results have been collected and compared with those obtained using BCA (Binary Collision approximation) methods, in order to find an analytical correlation which can predict the clustering process in SiC without using MD methods for larger range of PKA energies, reducing the total computational costs. The result of this study will be used to parameterize a higher scale object kinetic Monte Carlo method for direct comparison between the model and the experimentally observed microstructure under irradiation.

Keywords: Molecular dynamics; SiC; SiC fibers; Molecular statics; Multiscale modelling; OKMC; NRT formulas;

Negli ultimi anni, fibre al carburo di silicio sono state prese in considerazione come copertura per migliorare la resistenza dei fuel claddings in caso di incidente, mantelli e perfino materiali strutturali per reattori ad acqua e a fusione. In questo momento, grazie ad un fitto network di partecipanti al progetto Horizon 2020 IL TROVATORE® *in tutto il mondo, si sta ampliando la ricerca basata sullo studio sugli effetti e i danni su materiali innovativi come SiC/PyC (interfaccia di carburo di silicio e graphite) soggetti a irradiazione. In questa tesi, utilizziamo metodi atomistici per determinare la*

produzione di difetti e il loro accumulo in compositi SiC/PyC. Metodi di statica molecolare tradizionale (MS) sono utilizzati per caratterizzare l'interazione dei difetti puntuali in prossimità di difetti prodotti dall'irradiazione del materiale e altri difetti inerenti alle caratteristiche di base del materiale. Metodi di dinamica molecolare, invece, sono utilizzati per studiare l'effetto che l'interfaccia SiC/PyC ha sulla produzione di difetti nel carburo di silicio puro. I risultati relativi alla formazione dei difetti puntuali in SiC sono stati raccolti, analizzati e messi a confronti con gli altri ricavati dall'utilizzo di metodi tradizionali quali TRIM, SRIM e formule analitiche (NRT) in modo da determinare una correlazione matematica che predica la formazione di clusters nel cuore del carburo di silicio riducendo notevolmente il tempo di simulazione. Infine i risultati di questo studio saranno utilizzati come input per determinare l'evoluzione di questi difetti a lungo termine utilizzando programmi base Montecarlo (OKMC) per determinare affinità e differenze con eventuali futuri esperimenti.

Contents

Chapter 1

Chapter 2

Chapter 3

Chapter 4

Chapter 5

Chapter 6

List of figures

Chapter 1

Chapter 3

Chapter 4

Chapter 5

List of tables

Nomenclature

ASME	American Society of Mechanical Engineers
ASTM	American Society for Testing and Material
BOP	Bond Order Potential
C	Carbon
CM	Center of Mass
C_{Si}	Carbon antisite
DPA	Displacements per atom
DFT	Density Functional Theory
ES	Electronic Stopping (Power)
FP	Frenkel Pair
HTGR	High Temperature Gas Reactor
keV	10^3 elettronvolt
LOCA	Loss of Coolant Accident
MC	Monte Carlo method
MEAM	Modified Embebbed Atom Method
MD	Molecular dynamics
MS	Molecular statics
NRT	Norgett-Robinson-Torrens
OKMC	Object Kinetic Monte Carlo
PKA	Primary Knock-on Atom
PWR	Pressurized Water Reactor
Si	Silicon
SiC	Silicon Carbide
SiC/PyC	Silicon Carbide / Pyrolytic Graphite interface
Si_C	Si antisite
SIA	Self-Interstitial Atoms
SRIM	Stopping and Range of Ions in Matter

T89	Original Tersoff Potential (1989)
T90	Modified Tersoff Potential (1990)
T94	Modified Tersoff Potential (1994)
TDE	Treshold Displacement Energy
TEM	Transmission Electron Microscope
TRIM	Transport od Atoms in Matter
TRISO	Tristructural-isotropic
V	Vacancy
VHTR	Very High Temperature Reactor
ZBL	Ziegler-Biersack-Littmark

Chapter 1

1. Introduction

This introduction exposes the context of this work, pointing out the importance of this research thesis on industrial applications related to the use of SiC fibers, mainly in nuclear industry.

After the description of the main mechanical and thermic properties of SiC and SiC/PyC fibers, an outline of the thesis is given in order to introduce the overall topic to the reader.

1.1. SiC and SiC Composites

Silicon carbide, also called moissanite is found in only minute quantities in certain types of meteorite and in corundum deposits. Because of its rare occurrence in nature, all the silicon carbide sold in the world is synthetic. Natural moissanite was first found in 1893 as a small component of the Canyon Diablo meteorite in Arizona by Dr. F.H Moissan, after whom the material was named in 1905.

Silicon Carbide has been recognized as an ideal material for applications that require superior hardness, high thermal conductivity, low thermal expansion, chemical and oxidation resistance.

In the solid state, the stoichiometric composition of silicon and carbon termed silicon carbide (SiC) is the only chemical stable compound in the C/Si system.

More than 250 different types of structures, so-called polytypes of SiC exist [1]. The differences between all these compounds consist mainly in the stacking sequence of identical, close-packed SiC bilayers.

The Figure 1.1 shows the stacking sequence of the most common and technologically most important SiC polytypes, which are the cubic (3C) and hexagonal (2H, 4H and 6H) polytypes.

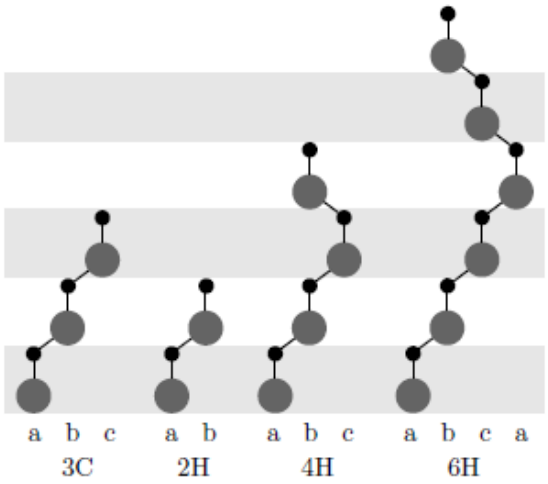

Figure 1.1: Stacking sequence of SiC bilayers of the most common polytypes of SiC (from left to right): 3C, 2H, 4H and 6H [2].

All polytypes have the phase diagram of the C/Si system in common, as shown Figure 1.1.2.

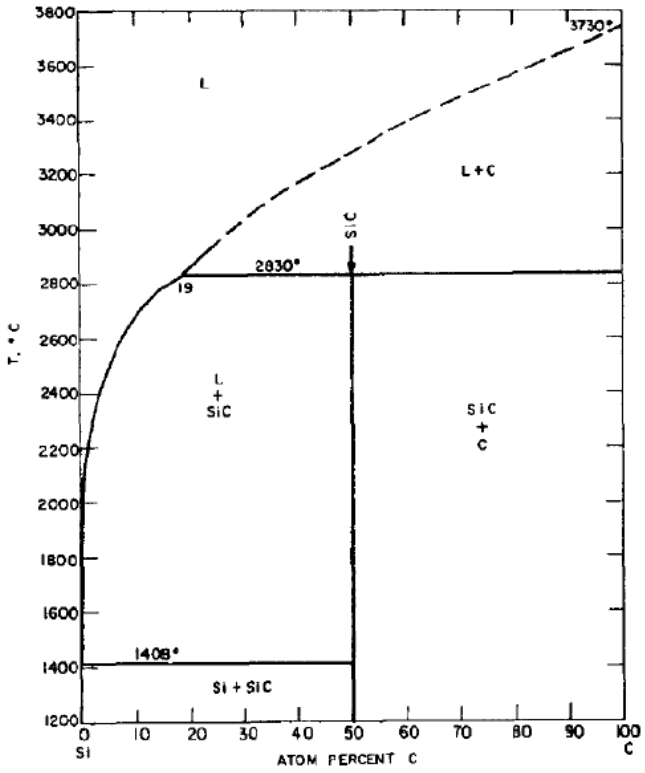

Figure 1.1.2: Phase diagram of the C/Si system [3]

Because of its high mechanical stability, heat resistance, radiation hardness and low neutron capture cross section, it is proposed for operation in harsh and radiation-hard environments, which make it a suitable candidate cladding (coating) material for nuclear fusion. A European project dedicated to the use of advanced carbides as coatings for accident tolerent fuels is the IL TROVATORE project, to which the present thesis contributes.

The low neutron capture cross section and radiation hardness favors its use in nuclear detector applications. In fact, the high breakdown field coupled with the high thermal conductivity allow SiC transistors to handle much higher power densities and frequencies in stable operation at high temperatures.

Moreover, in addition to high-temperature operations, the wide band gap also allows the use of SiC in optoelectronic devices: the SiC photodiodes serve as excellent sensors applicable in the monitoring and control of turbine engine combustion.

The Table 1.1 presents the major qualities and properties of 3C-SiC from mechanical and thermal point of view compared with diamond.

Properties/ Material	*SiC*	*Diamond*
Density [g/cm^3]	3.16	3.5-3.53
Melting Point [°C]	2830	Doesn't melt at ambient pressure
Solubility	Insoluble in water and molten metals, apart iron and alkalis compounds.	insoluble
Hardness [GPa]	35-45	70-80
Young Modulus [GPa]	448	1041
Thermal Conductivity [W/cm°C]	5	20
Bandgap energy [eV]	2.4	5.5

Table 1.1: Material properties of SiC compared with cubic diamond

Radiation effects in silicon carbide (SiC), whether in monolithic or composite forms (SiC/SiC), have been studied since the middle of the last century. In the past decade, this interest has grown, with the application of SiC in the nuclear fuels area continuing and new applications as potential structural materials gaining increasing attention.

The use of SiC in nuclear industry spaces in a broad range of nuclear applications, such as advanced nuclear fuel forms, structural components for fission reactor systems, blanket structures for fusion energy systems, and the immobilization of nuclear waste.

Pure monolithic and/or composite forms of SiC were first utilized in nuclear application as the micro-pressure vessel for gas-reactor fuel in the TRISO fuel form [4] [5]. In this regard, in the past decade many experiments have been carried out on SiC under neutron irradiation conditions at reactor relevant conditions, the interaction between the SiC layer and the surrounding pyrolytic carbon (PyC) layers under irradiation, and how to accurately model the performance of the TRISO particle under irradiation.

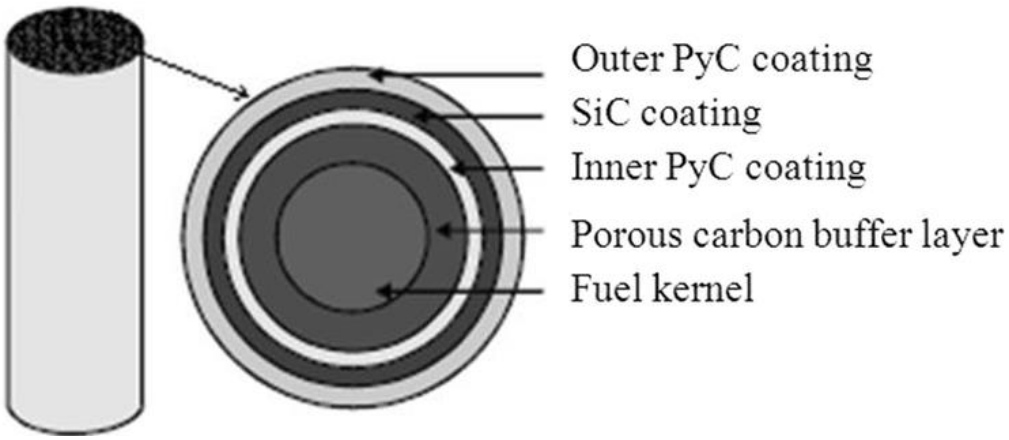

Figure 1.1.3: TRISO Fuel compact and coating fuel [4].

Moreover, the superior mechanical properties, high thermal conductivity, low thermal expansion, thermal shock resistance and chemical inertness of SiC are also important for its use in the immobilization of nuclear waste.

In the '80s, in fact, layers of pyrolytic carbon and silicon carbide were proposed as a coating to improve the separation and immobilization of cesium from the reprocessing of spent nuclear fuel.

Today, in all these nuclear waste applications, monolithic cubic 3C-SiC is the primary polytype of interest, for its long-term chemical durability and radiation response, which are important in retaining radionuclides in a geologic repository.

Within the core of LWR's, the use of SiC composites as fuel cladding and fuel channel boxes has been proposed. Specifically, the SiC composite has been proposed as a direct replacement for Zircaloy clad, which is hoped to offer significantly enhanced safety attributes in terms of Loss of Coolant Accident (LOCA) performance.

For safety reasons, under normal operating conditions, the thin walled tube should not release fission products to the coolant. For this purpose, recent studies indicate that neutron irradiation should not be an issue for the true matrix cracking stress or ultimate strength of SiC composites [6].

Moreover, the radiation properties of SiC composite are ideal for use as the channel boxes for a fuel assembly, since it has been found to isotropically expand by a little over 2% in volume [7]. For what regards Generation IV technologies, SiC/SiC composites are considered appropriate for HTGR/VHTR in-vessel components and SiC/SiC as a filler if necessary [8].

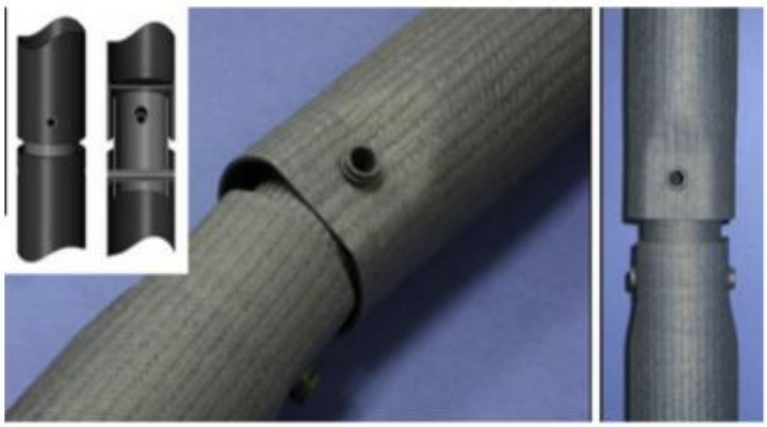

Figure 1.1.4: Prototype SiC/SiC control rods with articulating joints [8].

On the other hand, it has been seen that, a potentially important design-limiting issue for SiC/SiC composites in gas cooled reactor application is the time-dependent failure in a weakly oxidizing radiation environment due to impurities in the helium coolant [8].

Materials working in a future fusion reactor will be subjected to extreme temperature and radiation conditions, which are able to modify their properties. SiC-based composites, due to its inherent high-temperature capability (thus high potential thermal efficiency) and low induced radioactivity, is considered a key material in the development of fusion energy.
The international fusion program has sought to develop these ‘‘low activation’’ composites for fusion structures such as the first wall that faces the plasma, the divertor that intercepts the edge plasma, and the blanket that is the bulk of the structure and serves the purpose of breeding tritium fuel and managing a large fraction of the fusion power.
Reduced activation ferritic/martensitic steels, SiC/SiC composites and vanadium alloys are the three main candidate materials for blanket structures. SiC/SiC composites are

considered an advanced structural material because of their attractive safety features when used in a helium-cooled ceramic breeding (HCCB) blanket or self-cooled lead-lithium (SCLL) blanket.

In particular, the most significant achievement in this process was the development of exceptionally radiation-resistant SiC/SiC composites, which proved to not deteriorate the mechanical properties irradiated up to a high neutron fluence. This is especially true for SiC/SiC fibers enriched in oxides (e.g 30% $ZrSiO_4$, Tyranno-SA and Hi-Nicalon type-S), which show better high temperature and cracking resistance [8].

In general, the first wall undergoes the harshest irradiation damage in fusion devices. Moreover, because the radiation effect on lattice thermal conduction is inevitable, the radiation-induced decrease in thermal conductivity is a critical design-limitation for a ceramic first wall.

In conclusion, the future use of this material is mostly dependent on the creation of nuclear-specific ASTM standards and the creation of ASME design code development specifically dedicated to the application of these materials in all type of nuclear reactors.

1.2. Microstructural Evolution

Many authors in literature identified guidelines for ion irradiation to screen SiC/SiC for use in LWRs for ATF applications. For this specific use of SiC and/or SiC fibres in the nuclear sector, the assessment of the SiC/SiC composites is constrained to a narrow window of conditions: E =400-500 GPa, flexural strength = 300–450 MPa, flexural strain = 1–1.25%, and irradiation swelling = 1–2% in the 300–600°C range. In addition, the material has to demonstrate radiation stability up to a fast fluence of $20x10^{21}$ n/cm^2, or about 20 dpa.

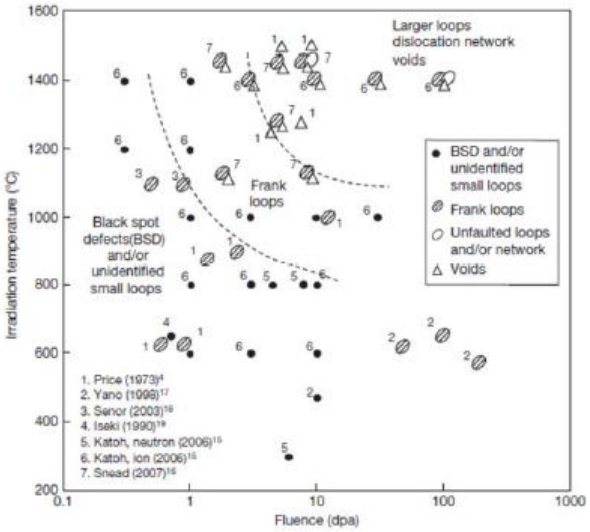

Figure 1.2.1: Microstructural features observed in SiC as function of temperature and damage (dpa) [9].

Initially, damage accumulates in SiC in the form of black spot defects or dislocation loops too small for adequate characterization. As either the temperature or dose (dpa) increases, interstitials gather to form faulted Frank loops. When both temperature and dose are increased, voids and unfaulted loops develop.

Qualitatively, similar microstructural features have been observed under neutron irradiation and silicon ion irradiation [10] in the form of black spot defects at low temperature, and dislocation loops and cavities at higher temperatures (>1250°C).

At 400°C, only interstitial clusters were identified. Clusters and small loops were present with diameters of 2.61 nm and 3.48 nm and densities of the order of 10^{23} -10^{24} m^{-3} for 600 and 800°C, respectively. At 1000°C, a majority of the loops presented as faulted Frank loops with average diameters of 5.25 nm and a lower density of 10^{22} m^{-3}.

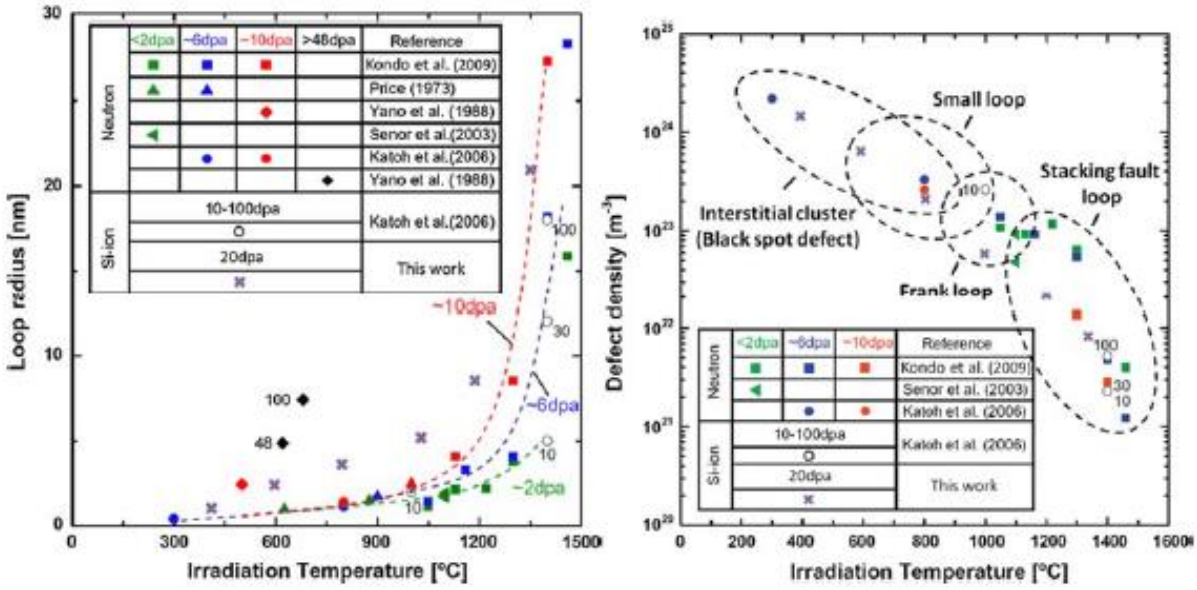

Figure 1.2.2: Dependence of defect radius (a) and defect density (b) on irradiation temperature in Si-ion and neutron irradiated 3C-SiC [11].

1.3. Swelling

At nearly all temperatures, SiC swells despite the lack of cavities at low temperatures and doses.

Below a critical temperature (about 150°C), swelling is primarily caused by amorphisation of the SiC material as strain accumulates from irradiation-induced defects from either self-ion irradiation or fast neutron irradiation.

In the intermediate temperature regime above the critical amorphization temperature (about 200°C) due to vacancy mobility (about 1000°C), swelling of cubic SiC under neutron irradiation appeared to saturate with irradiation dose and decrease with irradiation temperature for the same dose as shown in Figure 1.3.1.

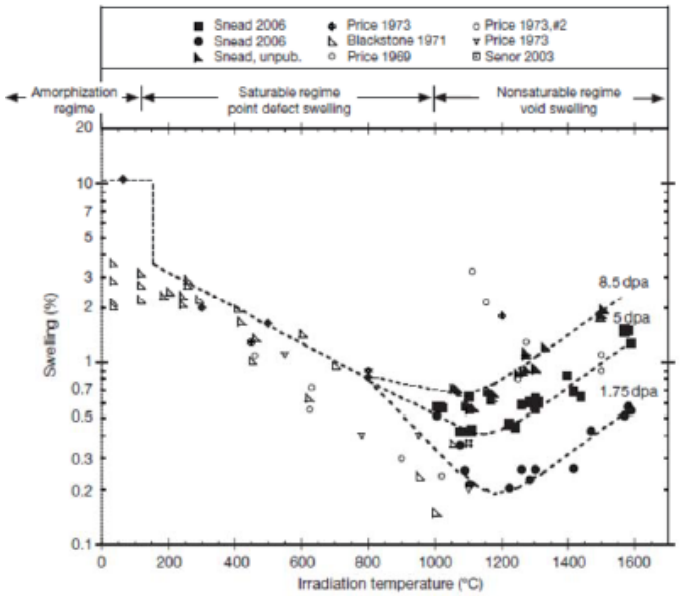

Figure 1.3.1: Irradiation-induced swelling of β-SiC for a wide temperature range [10].

These secondary phases were also reported in other irradiated SiC fibre composites and expected to be rich in carbon. The swelling of pyrolytic carbon (PyC) by amorphisation is expected at 300°C, as evidenced in the layers surrounding the fibres. The supporting SiC and PyC layers also appeared to mix and lose crystallinity, swelling from this amorphisation. The differential swelling between the interface and the matrix was also observed in ion irradiation at 300°C to 100 dpa [12].

1.4. Mechanical properties under irradiation

The experiments performed on irradiated cubic SiC samples and SiC fibres showed a slight decrease in the elastic modulus. It was also possible to say that the degradation of mechanical properties was dependent on the irradiation temperature. Nano-identation experiments showed that some of the samples subjected to the load failed, while some showed transition from an elastic to a plastic flow. This transition has been defined as a consequence of the irradiation effect on the fracture strength. In fact, irradiation-induced strengthening occurred. The engineering stress-strain curves showed that irradiation-

induced strengthening seemed to be significant between 300 and 800 °C. As explained in the previous section, the observed microstructures of ion-irradiated SiC showed the appearance of small clusters when the temperature reaches 400°C. These defects, are expected to affect the mechanical properties and induce various radiation effects.

As well as pure SiC, SiC/SiC composites show the degradation of mechanical properties when subjected to irradiation, in particular showing the reduction of the Young's modulus, ranged 5– 20% in most cases. The reduction increases with irradiation temperature, as shown in Figure 1.4.1.

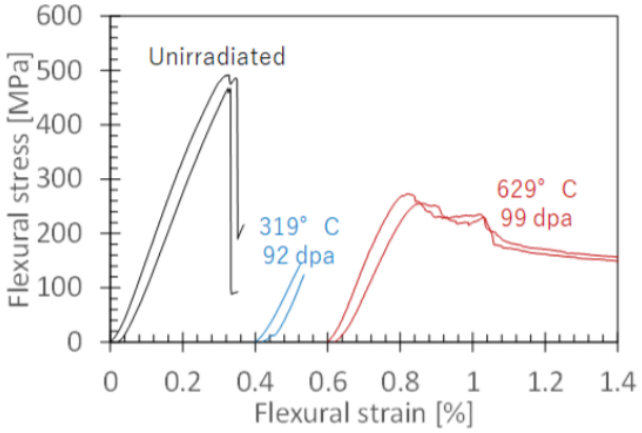

Figure 1.4.1: Flexural behavior of non-irradiated and irradiated CVI SiC/SiC composites. The stress-strain curves are shifted to aid visibility [13].

Similar behavior is shown by PyC/SiC interfaces, which showed a the degradation of PyC interphase.

There are several considerations when designing any ion irradiation campaign. The first step is to determine what information can be achieved with the desired technique. The use of ion irradiation to emulate neutron irradiation in SiC is not limited by the ability to assess the microstructure, but by the ability to measure the bulk mechanical properties associated with the ion irradiated microstructure. That's why there is the need for predictive tools to complement and steer experiments.

1.5. SiC degradation under irradiation: a problem of multi-scale modelling

As these materials are degraded by their exposure to high temperatures, irradiation and a corrosive environment, it is necessary to address the issue of long term degradation of materials under service exposure in advanced plants.

Thus, irradiation damage becomes a multi-scale problem: A higher confidence in life-time assessments of these materials requires an understanding of the related physical phenomena on a range of scales from the atomic level of single defect energetics all the way up to macroscopic components.

Recently, there has been a surge to study materials using multiscale modelling, by performing studies using a wide range of techniques. This has come about with the recognition that the macroscopic failure of a component is associated with events that start at the atomic level. The multiscale modelling, in fact, intends to follow the development of phenomena that originate at the atomic level using appropriate modelling schemes, all the way to the macroscopic level. This procedure enables physical insight into the material's behavior, which might otherwise be lost if only experimental correlations are used. Experiments are then needed to test or validate critical aspects of the modelling.

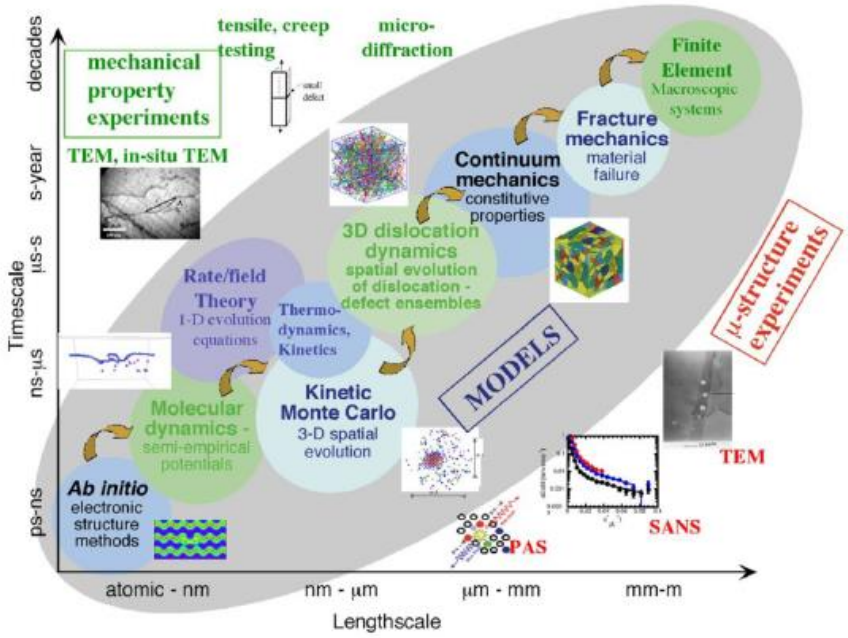

Figure 1.4.2: Schematic representation of different modelling techniques in the multiscale modelling chain as a function of time and length scale [14].

The basics building block of the damage produced by an irradiating particle is the displacement cascade, produced by a recoil atom induced by the incoming energetic particle. The highly energetic and disordered region produced in the crystal, is partially annealed out in the order of picoseconds, mainly through non-diffusive recombination of defects at its core. A high concentration of defects, both single vacancies, interstitials and their clusters are left behind after the self-annealing process. It is the evolution of these defects and their diffusion to different sinks (dislocations, grain boundaries and other interfaces) that is responsible for the fluxes that modify the local composition and microstructure of the material. The timescales of this initial damage evolution are such that it can only be accessed by modelling.

The multiscale modelling method encompasses an atomistic description of forces between atoms using ab initio calculations and molecular dynamics (MD), which uses these interatomic forces as input, and then move to kinetic Monte Carlo (KMC), which uses the results of the previous two calculations as input to reach even longer atomistic time and

length scales. Modelling of the mechanical properties of the material is achieved by implementing dislocation dynamics (DD) simulations and the proper macroscopic scale then uses finite element (FE) methods and continuum models.

Thus, the interchange between computational models and experiment is critical in developing accurate predictive models. Improvements of micro- and nanostructural investigation methods (quantitative electron microscopy and microanalysis), high resolution transmission microscopy, atomic force microscopy, X-ray technologies, together with specimen preparation (like FIB) are allowing a direct coupling of the local mechanical properties with the local microstructure.

To contribute to this topic, the present thesis focusses on primary damage production and defect interface interactions. Large-scale molecular dynamics (MD) simulations have been applied to study defect production for lattice atom recoil energies in the range 1-100 keV, caused by primary knock-on atoms (PKAs) in 3C-SiC. Finally size and composition distribution of in-cascade clusters provide a critical input for long-term defect evolution models. Molecular static simulations have been employed to estimate the binding erergy between different point defects and SiC/graphite interface. Also these results provide input for long-term defect evolution models.

Chapter 2

2. Objectives and work plan

The objectives of the present thesis are twofold:

I. perform an in-depth MD study to characterize primary damage in SiC;

II. initiate a study to characterize the binding energy between point defects and the SiC/graphite interface.

Both objectives will provide direct input to coarse grain models such as object kinetic Monte Carlo and rate theory models.

To reach these objectives, the following work plan is followed:

- **Potential selection**

Amongst different potentials available in the literature we computed the energetic stability of point defects (vacancy/interstitial/anti-sites) in both 3C-SiC and graphite. The results were compared with available DFT data and the potential providing best agreement with DFT was retained for further studies.

- **Stiffening of the selected potential**

Once the most appropriate equilibrium potential is selected, it needs to be stiffened to correctly reproduce the electronic and nuclear stopping power. For the nuclear stopping power the potential was smoothly merged to the ZBL screened Coulomb potential such that the equilibrium properties were not modified. For the electronic stopping, a viscous friction term was introduced in the MD integration algorithm such that the electronic stopping power predicted by SRIM is reproduced.

- **Cascade simulations using MD**

Using the stiffened potential and the appropriate viscosity term, cascades were simulated for PKA energies in the range 1-100keV along high index directions at zero Kelvin. Each condition was simulated 10 times to achieve statistics.

- **Analysis of the MD results**

Defect analyses are performed on the MD results to characterize the cascades in terms of produced Frenkel pairs, anti-sites and vacancy/interstitial clusters. Regressions as a function of PKA energy were derived.

- **Cascade simulations using BCA**

The BCA method and NRT formula were applied and their defect production compared to the MD results. The aim is to reliably estimate the total defect production based on BCA/NRT methods, while their clustering probability is obtained from the regressions based on the MD results.

- **Initiation of defect/interface interactions**

Molecular static calculations were performed to estimate the binding energy between point-defects and different SiC/graphite interface configurations.

Chapter 3

3. Methods

3.1 Molecular statics

Atomistic simulations describe materials at the level of atoms. In the case of Molecular Statics (MS), the relaxed configuration of atoms is found using a conjugate gradient or some similar (constrained) minimization of the total energy. This provides information about crystal lattice structure in different phases and under different conditions.

3.1.1 Correlation Force/Energy

For any potential U(r) ,force exerted on atom *i* due to atom *j* is given by the following equation

$$\overline{f} = -\nabla U\left(r_{ij}\right) \tag{3.1}$$

Then we have total force exerted on a particular atom

$$F = \sum_{r_{ij} < r_c} f_{ij}(r_{ij}) \tag{3.2}$$

Finally, the potential energy of atom i directly given by the potential

$$E_i^u = \sum_{r_{ij} < r_c} U\left(r_{ij}\right) \tag{3.3}$$

The equilibrium state of the lattice corresponds to the global minimum of its potential energy. Generally, at each step the unbalanced resultant forces acting on each atom are found. Then each atom is moved into the direction of the unbalanced force vector by the amount functionally dependent on the magnitude of this force.

3.2 Molecular Dynamics

MD simulates the time evolution of a system of classical particles by repeatedly solving Newton's second law of motion for each individual particle; on an atomistic scale, it simulates the trajectories of individual particles rather than bulk properties of the material. Assuming that at some time t_i, the positions $r(t_i)$, velocities $v(t_i)$, and masses m of the particles are known, the MD algorithm will proceed as follows:

1. Using a provided potential V (r_0, r_1, r_2…), the net force $F = -\nabla V$ on each particle is computed at time step t_i.
2. Using Newton's second law F = ma, the acceleration of each particle is computed at time step t_i.
3. Using the acceleration $a(t_i)$, the position $r(t_i)$, and the velocity $v(t_i)$ the position and velocity of the particles at the next time step, $r(t_{i+1})$ and $v(t_{i+1})$, are computed.
4. Steps 1-3 are repeated for time step t_{i+1}

3.2.1 LAMMPS

LAMMPS (Large-scale Atomic/Molecular Massively Parallel Simulator, see http://lammps.sandia.gov), an MD program developed by Sandia National Laboratories, was used in this project to simulate the effect of PKA energy on defect production on irradiated SiC and SiC/graphite interface. LAMMPS utilizes parallel computing to simulate collections of atoms and/or molecules using standard molecular dynamics code [15]. At the end of the simulation, LAMMPS outputs a text or dump file containing the coordinates and energies of all particles in the manually built simulation box, as well as any other parameters that the user requests. In this project, for each atom in the simulation, LAMMPS outputs the atom ID, the location, the potential energy. These outputs were then used in OVITO, along with some of OVITO's [16] analysis methods, to analyze the defects in each simulation.

3.3 Periodic Boundary Conditions

For a system to remain homogeneous in space one applies periodic boundary conditions. When using PBC, particles are enclosed in a box, in such a way we can image that it is replicated to infinity by rigid translation in all the three cartesian directions, completely filling the space. In other words, the cells adjacent to the central simulation cell are periodic images of it. In Figure 3.3.1 particles that move out through one face of the cell are replaced by their images coming in through the opposite face. For example, particle 1 moves out of the right-hand face of the central simulation cell and is replaced by particle 1’ coming in from the left image box. The interactions between particles are calculated such that an atom interacts with its closest image.

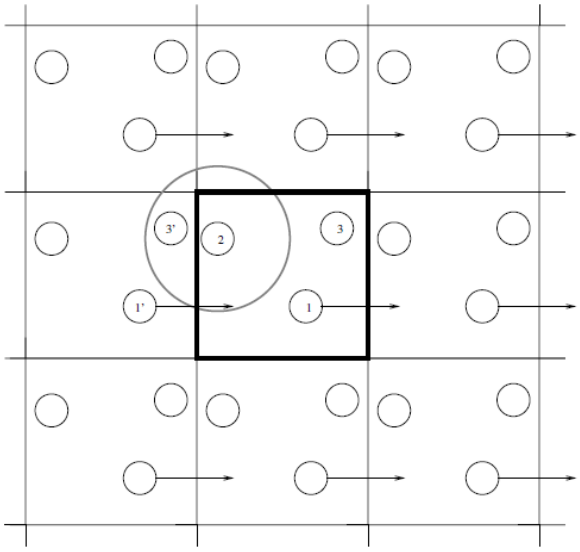

Figure 3.3.1: The square periodic boundary conditions commonly used for equilibrium molecular dynamics simulations as 2D representation. The central cell (bold) is the primary cell and the cells surrounding it are its periodic images. Particles 1' and 3' are periodic images of particles 1 and 3, respectively [17].

Periodic boundary conditions are implemented as,

$$F\left(r + L\left(n_x n_y n_z\right)\right) = F(r) \tag{3.4}$$

where nx, ny and nz are integers. [18].

3.4 Potentials: General Overview and Formalisms (MEAM/Tersoff)

The potential energy of N interacting atoms can be written in the form

$$U(r) = \sum_i U_1(r_i) + \sum_i \sum_{j>i} U_2(r_i, r_j) + \sum_i \sum_{j>i} \sum_{k>j>i} U_3(r_i, r_j, r_k) \ldots \quad (3.5)$$

where U is the total potential energy. U_1 is a single particle potential describing external forces. Examples of single particle potentials are the gravitational force or an electric field. U_2 is a two body pair potential which only depends on the distance r_{ij} between the two atoms i and j. If not only pair potentials are considered, three body potentials U_3 or many body potentials Un can be included. Usually these higher order terms are avoided since they are not easy to model and it is rather time consuming to evaluate potentials and forces originating from these many body terms.

In our work we used three-body potentials in form of MEAM and Tersoff type potentials.

3.4.1 MEAM Potential

The MEAM was created by Baskes, by modifying the EAM so that the directionality of bonding is considered, and was applied to provide interatomic potentials of various fcc, bcc, diamond, and gaseous elements [19].

The general MEAM formalism can be expressed as following:

$$U = F_i(\bar{\rho}_i) + \frac{1}{2} \sum_{j \neq i} \Phi_{ij}(R_{ij}) \quad (3.6)$$

F_i is the embedding function, $\bar{\rho}_i$ is the background electron density at site i, and $\Phi_{ij}(R_{ij})$ is the pair interaction between atoms i and j separated by a distance R_{ij}. Within EAM the background density has a central symmetry, while in MEAM, it depends on the angle formed between two nearest neighbor atoms from atom i.

3.4.2 Tersoff Potential

Tersoff proposed an empirical interatomic potential for covalent systems [20][21]. The Tersoff potential explicitly incorporates the dependence of bond order on local

environments, permitting an improved description of covalent materials. Due to the covalent character, Tersoff restricted the interaction to nearest neighbor atoms accompanied by an increase in computational efficiency for the evaluation of forces and energy based on the short-range potential. Tersoff applied the potential to silicon [20], carbon and also to multicomponent systems like silicon carbide [21].

Tersoff incorporated the concept of bond order in a three-body potential formalism. The interatomic potential is taken to have the form

$$E = \sum_i E_i = \frac{1}{2} \sum_{i \neq j \neq} V_{ij} \qquad (3.7)$$

$$V_{ij} = f_c(r_{ij})[V_R(r_{ij}) + b_{ij} V_A(r_{ij})] \qquad (3.8)$$

E is the total energy of the system, constituted either by the sum over the site energies E_i or by the bond energies V_{ij} . The indices i and j correspond to the atoms of the system with rij being the distance from atom i to atom j. The functions V_R and V_A represent a repulsive and an attractive pair potential. The repulsive part is due to the orthogonalization energy of overlapped atomic wave functions.

In case of the Erhart-Albe potential, the repulsive and attractive terms change slightly form the original formalism in the following way:

$$V_R(r) = \frac{D_0}{S-1} \exp[-\beta\sqrt{2S}(r - r_0)] \qquad (3.9)$$

$$V_A(r) = \frac{SD_0}{S-1} \exp[-\beta\sqrt{2/S}(r - r_0)], \qquad (3.10)$$

where D_0 and r_0 are the dimer energy and bond length. The parameter b can be determined from the ground-state oscillation frequency of the dimer, while S is adjusted to the slope of the Pauling plot. The cutoff function is defined as,

$$f_C(r) = \begin{cases} 1 & r < R - D \\ \frac{1}{2} - \frac{1}{2}\sin\left(\frac{\pi}{2}\frac{r-R}{D}\right) & |R-r| \leqslant D \\ 0 & R + D < r \end{cases} \tag{3.11}$$

The parameters R and D specify the position and the width of the cutoff region. The bond-order is given by

$$b_{ij} = (1 + \chi_{ij})^{-1/2} \tag{3.12}$$

with

$$\chi_{ij} = \sum_{k(\neq i,j)} f_C(r_{ik}) \exp[2\mu(r_{ij} - r_{ik})] g(\theta_{ijk}) \tag{3.13}$$

and the angular function

$$g(\theta) = \gamma\left(1 + \frac{c^2}{d^2} - \frac{c^2}{d^2 + [h + \cos\theta]^2}\right). \tag{3.14}$$

The three-body interactions are determined by the parameters 2μ, γ, c, d, and h, which leads in total to up to nine adjustable parameters, all of them depending on the type of atoms i and j.

The parameter optimization proceeds as follows: First, the pair parameters are adjusted to the dimer properties D_0, r_0, β and the slope of the Pauling plot(S). Thereafter, the three-body parameters are fitted to the cohesive energies and bond lengths of several high-symmetry structures as well as to the elastic constants of the ground structures. The

transferability of the potential is enforced by including a variety of differently coordinated structures in the fitting database [22].

3.4.3 Stiffening of the potential to ZBL for short range interaction

In case of high energy events, such as simulations of collision cascades due to high energy ion irradiation, the repulsive potential can be modified to give a more accurate behavior at interatomic distances much shorter than in typical near-equilibrium simulations. Another repulsive function, $V_{R0}(r)$, in addition to the original $V_R(r)$, is often included as

$$V_{ij}^{ZBL} = \frac{1}{4\pi\epsilon_0}\frac{Z_1 Z_2 e^2}{r_{ij}}\phi(r_{ij}/a) \tag{3.15}$$

$$a = \frac{0.8854\, a_0}{Z_1^{0.23} + Z_2^{0.23}} \tag{3.16}$$

$$\phi(x) = 0.1818e^{-3.2x} + 0.5099e^{-0.9423x} + 0.2802e^{-0.4029x} + 0.02817e^{-0.2016x} \tag{3.17}$$

the total potential energy of a system of atoms is given by

$$V_{ij} = (1 - f_F(r_{ij}))V_{ij}^{ZBL} + f_F(r_{ij})V_{ij}^{Tersoff} \tag{3.18}$$

Where f_f represents the short-range function through the use of the Fermi function

$$f_F(r_{ij}) = \frac{1}{1 + e^{-A_F(r_{ij} - r_C)}} \tag{3.19}$$

The use of this function allows for a smooth connection between the equilibrium potential and the short range ZBL potential.

The total potential is dominated by the ZBL profile for a short distance and quickly approaches the BOP as r increases. A_F and r_C are defined not to chane the equilibrium energetics of the potential. We identified A_F with 28 A^{-1} and r_C with 0.95 A for Si-C interactions.

3.4.4 Defect Analysis Using OVITO

In order to analyze the raw text output of the LAMMPS simulations, OVITO (Open Visualization Tool) was used. OVITO is a program that allows users to visualize the atoms in a simulation, as well as identify defects in the structure using a variety of methods. The methods used in this thesis are described in detail below.

• *Scalar Techniques:* This technique consists in characterize each atom using a single number.

• *Energy Threshold*: The simplest way of characterizing atoms using OVITO is to use their potential energy. The basis of this method uses the idea that a defect atom will have a higher energy than its surrounding perfect crystal structure neighbors, leading to the expectation that all atoms with energies higher than the perfect crystal energy for that material are defective.

• *Wigner-Seitz Analysis Modifier:* Wigner-Seitz analysis is a method in which Frenkel pair defects (i.e. interstitials and vacancies) and clusters of these defects (e.g. interstitial loops) can be identified in a structure by comparing it to a reference structure. This reference structure is a perfect crystal, meaning there are no defects and no displacement of atoms. Using the reference crystal, Wigner-Seitz cells are constructed around each atom; these cells are created by joining a set of planes that lie at the midpoint of and perpendicular to the lines linking an atom to its nearest neighbors [23].

3.5 Definitions

Characteristic energy values

One of the main objectives of this work is to study the evolution of point defects and clusters in irradiated SiC and SiC/graphite interface. In order to do that, it is first necessary to define some characteristic energy values that give information about the stability of the material crystallographic configuration or will tell us if a particular transformation is thermodynamically favored. It is therefore crucial to have a precise definition for each of these energies.

- *Cohesive energy*: it is the difference between the energy of a solid and the energy of the isolated atoms. In practice, it can be calculated using the following equation:

$$E_{coh} = \frac{E_{tot,system}}{N} - E_i \tag{3.20}$$

In our case $E_i = 0$ and N is total number of atoms in the system.

- *Binding energy*: when more than one lattice defect exists, they may repel or tend to cluster; if they cluster, it is because the total energy decreases when they join: the corresponding energy gain is called binding energy. It is calculated using atomistic simulation techniques as the difference between the energy the crystal when the defects are far (configuration A) and the same crystal when the defects are closer from each other (configuration B):

$$E_{binding} = E_A - E_B \tag{3.21}$$

- *Formation Energy*: the defect formation energy is how much cohesive energy is needed to form a point defect in a perfect lattice.

The formation energies E_f were obtained from the total energies of the supercells with a defect

$$E_f = E_d - E - \sum_i N_i \mu_i \quad (3.22)$$

E_d is the total energy of the defected supercell and E the total energy of perfect graphite and perfect cubic silicon boxes, which we calculated for supercells of the same size as used in the runs with the defects. N_i represented the total number of species in the supercell and μ in this formula is the pure cohesive energy of Si bulk and graphite bulk.

Following the method described by Erhart and Albe [22]. The formation energy reduces then to

$$E_f = E_d - \left(n_{Si} + n_C\right) \cdot \mu_{SiC,bulk} - \frac{1}{2}\left(n_{Si} - n_C\right)\left(\mu_{Si,bulk} - \mu_{C,bulk}\right) \quad (3.23)$$

In the case of graphite the formula reduces to

$$E_f = E_d - E - N_c \mu_C \quad (3.24)$$

Where N_c is the total number of atoms after the insertion of vacancy ($N_{perfect}$ -1) or interstitials ($N_{perfect}$ +1).

3.6 Simulating cascades

Our simulations used the variable time step procedure, based on the phases of cascade formation. We performed 10 different cascades for each energy simply changing the seed number which changes slightly the track and the velocity along one coordinate of the direction. Each cascade was reached about 20 ps.

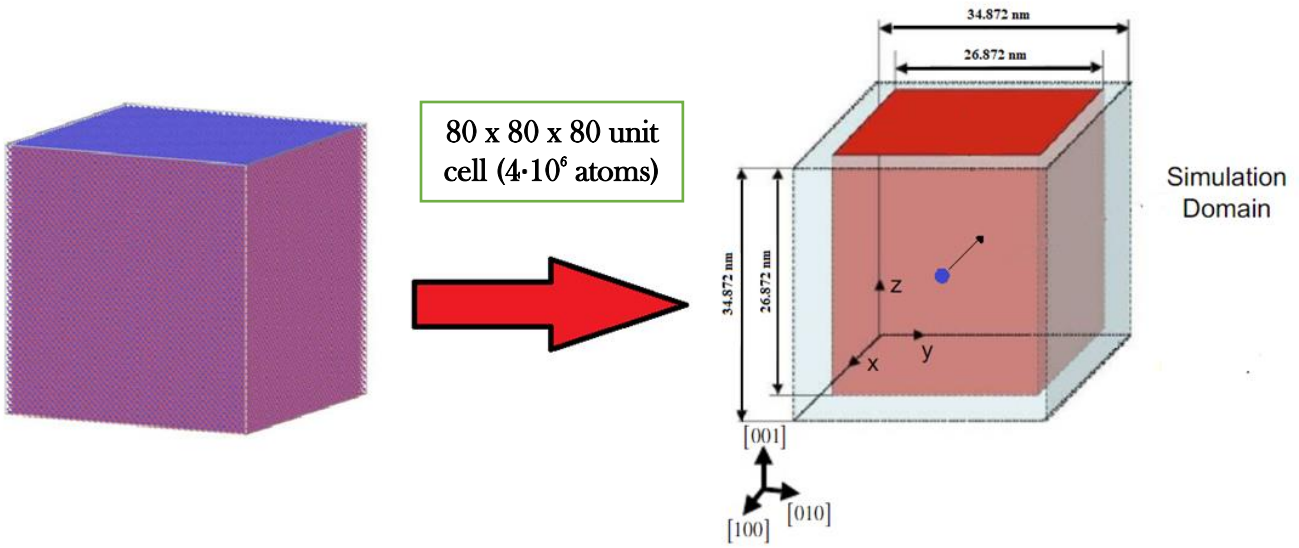

Figure 3.5.1: Representation of the simulation domain: from the reference state represented Ovito to the cascade event simulation

In this study we applied ZBL-EA(05) potential to 1keV, 5keV, 10keV, 50 keV and 100 keV cascade simulation in 3C-SiC cells. Our simulation consists in 80 x 80 x 80 3C-SiC unit cell (roughly $4*10^6$ atoms) for PKA energy until 10 keV, 100 x 100 x 100 3C-SiC unit cell ($8*10^6$ atoms) for PKA energy of 50 keV and 200 x 200 x 200 unit cell ($64*10^6$ atoms) for PKA energy of 100 keV. To simulate the bulk of an infinite body being at known energy we set the NVE ensemble. If the total number of atoms N and the volume V (of the unit cell) are also kept constant, then the MD simulations are said to be performed in the microcanonical (NVE) ensemble. Moreover, for large NVE systems the fluctuations in temperature are small, and it may be considered approximately constant. An NVT thermostat is defined in order to allow the system to thermally equilibrate for 1 ps prior to exciting the primary knock-in atom (PKA).

The recoil energy of PKA can be computed with the energy-angular distribution of the secondary particle.

The incident and emitted energies (velocities) are referred respectively to E and E' ($v0$ and v'). E_R (v_R) stands for the recoil energy (velocity) of the target. m and v_1 (m' and $u1$) are respectively the mass and velocity of incident (outgoing) particle. M and v_2 (M' and

u_2) are respectively the mass and velocity of the target particle before (after) the collision particle in the CM frame.

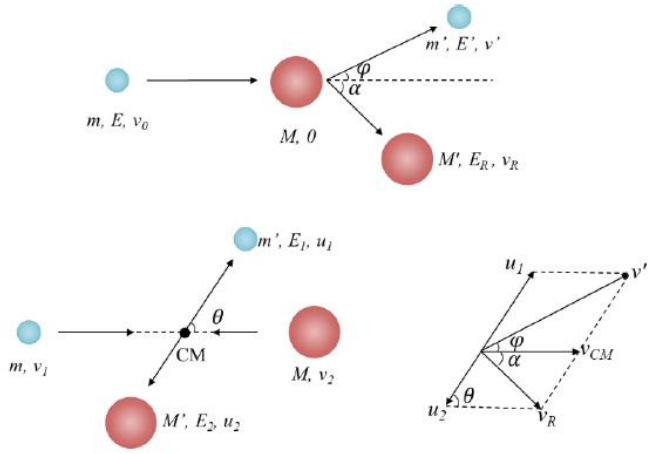

Figure 3.5.2: Schemes of the collision events

The relativity effect can be neglected in our studies that focus on energies lower than 20 MeV. The conservation of momentum points out:

$$mv_0 = m'v'cos\varphi + M'v_R cos\alpha, \tag{3.25}$$

$$m'v'sin\varphi = M'v_R sin\alpha. \tag{3.26}$$

By eliminating α ($\cos^2\alpha + \sin^2\alpha = 1$) using the conservation of momentum, the recoil energy of PKA is obtained as:

$$E_R(E, E', \tilde{\mu}) = \frac{1}{M'}[mE - 2\sqrt{mm'EE'}\tilde{\mu} + m'E'] \tag{3.27}$$

Where $\tilde{\mu}$=cosφ.

Performing very fast calculation, considering a range of neutron interaction between 0.025 eV and 2 MeV, and imposing that the neutrons loses entirely its energy after the collision (which is improbable in reality) and the angle of scattering is 0°, we obtain that the recoil energy of the Si atom approaches 100 keV.

That's why we decided to take into account 5 sets of energies: 1keV, 5 keV, 10 keV, 50 keV and 100 keV.

The total velocity of the PKA atom is

$$v_{Si} = \sqrt{\frac{2 \cdot E_{k,i}}{M_i}} \tag{3.28}$$

It velocity, chosen in accordance to what proposed in the work of Samolyuk et al. [24] is calculated close to <1 3 5> direction as defined in the table.

Energy	X direction	Y direction	Z direction
1 keV	140.11	420.33	700.55
5 keV	313.29	939.88	1566.47
10 keV	443.06	1329.19	2215.32
50 keV	990.72	2972.17	4953.61
100 keV	1401.09	4203.28	7005.47

Table 3.6.1: Velocity of Si-PKA atoms along the <1 3 5> direction

In order to increase the accuracy of our results, we have considered the evolution of the system with the influence of the electronic and nuclear stopping power.

We suggest that taking electronic stopping (ES) into account in MD simulations provide results closer to the experimental yields. ES refers to the energy loss through inelastic interactions between the electrons and the atoms in the materials under irradiation. It is a subtle but important issue in ion–solid interactions, but nearly all the previous simulations of keV large cluster bombardments on 3C-SiC have ignored it.

3.7 Evaluation of the electronic stopping with SRIM

Linear stopping power (stopping force) is defined as $S = -dE/dx$, where E is the ion energy and x is the path length. We often use the mass stopping power S/ρ, where ρ is the mass density of the material.

- Electronic stopping (collisions between ion and target electrons) leads primarily to excitation and ionization of target atoms, and to energy loss of ion.
- Nuclear stopping (elastic "billiard ball" collisions between ion and target atom) leads to change of direction, and to energy loss of ion. (No nuclear forces are involved!)
- The total stopping power is the sum of nuclear and electronic stopping power:

$$S_{tot} = S_{el} + S_n \tag{3.29}$$

In order to incorporate the electronic stopping power in MD simulation, we have to calculate the friction term which modifies the velocity of the incoming particle in the system.

Knowing from the Newton law the dumping force is given by:

$$m \cdot \frac{d^2\vec{r}}{dt^2} = \vec{F} = \overrightarrow{F_{nuc}} + \overrightarrow{F_{el}} = \gamma \cdot \frac{d\vec{r}}{dt} \tag{3.30}$$

The larger the coefficient (γ), the faster the kinetic energy is reduced. The nuclear stopping power is already accounted for by the ZBL screened Coulomb potential.

3.8 Comparison between MD methods and BCA methods for radiation damages

3.8.1 BCA

One of the widely accepted techniques utilized for studying ion irradiation induced damage on surfaces, which is important at higher energies, is the Binary Collision Approximation (BCA). In BCA the assumption is made that collisions between atoms can be approximated as elastic binary collisions. In this technique, a single collision between the incident ion and a substrate atom is evaluated by solving the classical scattering integral between two colliding particles (the interatomic potential is usually a screened Coulomb potential).
The solution of the integral results in both the scattering angle of the incident ion and its energy loss, which is transferred to the substrate.

BCA methods use a maximum impact parameter set by the density of the medium and a constant mean free path between collisions. The scattering angle is determined by a specific formula, tested against published integral tables and represents the scattering from the ZBL "universal" potential seen previously in the chapter dedicated to the short range fitting of the BOP used in MD simulations.

The advantages of BCA is its speed, which is 4-5 orders of magnitude faster than MD [25]. Therefore BCA is based on some assumptions and limitations. This approximation emerges when incident ions have low energies, or in very dense substrate materials, or when chemical effects play a role in materials.
A static Monte-Carlo program which is known as transport of ions in matter is (TRIM). The program assumes an amorphous substrate structure at zero temperature and infinite side size and treats the bombardment of incident ions on different substrate structures [26]. Stopping and Range of Ions in Matter (SRIM) code [see: http://www.srim.org/] is another program which can calculate interaction of ions with matter. The core of SRIM is TRIM.

In the table below the major differences between traditional MD and BCA methods are listed:

MD	BCA
Advantages	
In MD simulations the system of atoms evolves by solving numerically the equations of motion. This method simulates the full many-body dynamics in atomic system → MD methods describe the interactions involved in ion implantation more realistically compared to other computer simulation methods	Its speed, which is 4-5 orders of magnitude faster than MD
More accurate for low energetic collisions	This can be used for large scale sampling and to compute an useful statistics.
Molecular dynamics can predict a huge amount of defects: vacancies, interstitials, antisites, dislocations, clusters, loops… and it is very effective for continuous motion problems	The CPU time required for simulating cascades is found several orders of magnitude smaller in the BCA than by full MD
The response of the local environment is explicitly taken into account in the MD which can have a substantial effect on the trajectory of the PKA.	The BCA can treat large system of more than 1 million particles
MD takes into account all stages: at the first stage, a very rapid recombination takes place that is apparently connected with the recombination of nearby pairs. At the second	For each collision, the classical scattering integral is solved for a given impact parameter between the moving atom and a stationary atom in the target material. The impact parameter is chosen randomly within the radius of the circular

stage, relaxation occurs much more slowly under the conditions of diffusion controlled reaction.	area of interaction cross-section and is calculated based only on composition and atomic density of the target material
Disadvantages	
MD is limited in the size of systems that it can model and require much larger computer capacity	This method approximates the full atomic dynamics of a material by a series of binary collisions, neglecting possible many body effects.
It shows results for a short time span (few ps)	Unlike MD, the BCA approach becomes less accurate with decreasing kinetic energy in the collisions, where multi-body interactions can become significant
The MD is not applicable for simulations of atoms in high energy because of the following three reasons: the MD simulation does not treat inelastic interactions by electron excitation. In general, the inelastic interactions cannot be ignored at high energy scattering. The MD simulation calculates the time evaluation by numerical integration and he time step has to be reduced to treat high-speed atoms. Moreover the MD has difficult to threat systems with more than 10 thousands atoms	It is difficult to devise structural perturbations and BCA does not take into account recombination processes, giving less precise statistics on the defects count

3.9 Threshold displacement energy in SiC

The Treshold Displacement Energy (TDE) is the minimal PKA energy on a certain direction required to form a stable Frenkel pair.

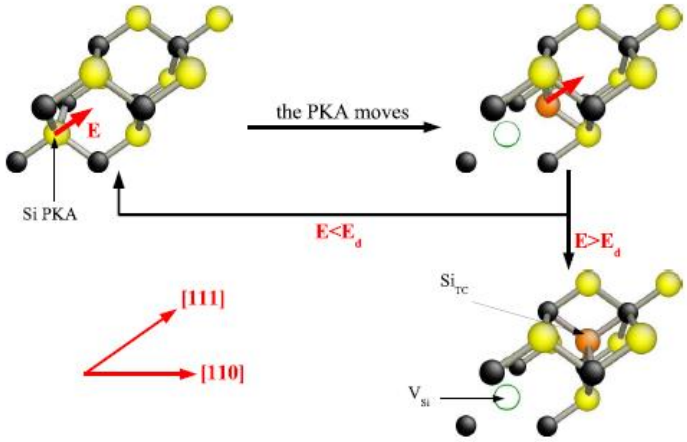

Figure 3.9.1: A Si PKA along the [111] direction. Carbon atoms are drawn in black, and silicon toms in yellow. The silicon PKA is drawn in orange and the vacancy is represented by an open circle. A kinetic energy E is given to a Si atom, which is subsequently displaced. If E<E_d, the PKA returns to its original location. If E>E_d, there is formation of a silicon vacancy VSi and a silicon tetrahedral interstitial surrounded by four carbon atoms Si_{TC}. [27].

This is typically taken as the smallest applied kinetic energy (i.e. a MOMENTUM in a given direction) required to displace an atom, and varies with crystallographic direction. In this section we compare the threshold energies found in this work with those found by other authors for both Si and C PKA.

As is commonly done in the literature, a weighted average was calculated to get an idea of the TDE over the range of PKA directions. This average can then be considered as a 'material average' TDE for each PKA type, taking into account the crystallographic symmetry of the material. This weighted average is calculated in the following manner,

$$TDE_{ave} = \frac{1}{\sum_i^{ndir} w_i} \sum_i^{ndir} w_i \cdot TDE_i \qquad (3.31)$$

where the weight, w_i , is the number of directions that are equivalent to those explicitly simulated, n_{dir} is the number of directions explicitly simulated and the first term is the total number o equivalent directions. For the 3C-SiC considered here, there are 6 <001>

directions 4 <111> directions, 4 $< \bar{1}\,\bar{1}\,\bar{1} >$ and 12 <110> directions. Thus $n_{dir} = 3$, $w_1 = 6$, $w_2 = 4$, $w_3 = 4$ $w_4=12$ and the total number of equivalent directions is 26.

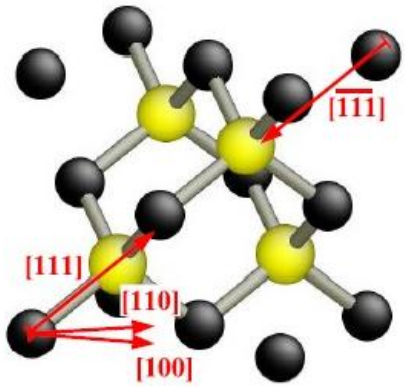

Figure 3.9.2: Representation of the main crystallographic directions in 3C-SiC [100] direction. Carbon atoms are drawn in black, and silicon atoms in yellow [27].

Hereafter, the results of this work have been compared with available DFT data and experiments collected by Lucas [43], Honsvet et al. [28] and Zinkle-Kinoshita [29].

PKA atom	Directions	This work	Lucas (DFT)	Hønstvet (DFT)	Zinkle-Kinoshita (TEM)
Silicon	[001]	34	46	45	45
	[110]	58	45	45	45
	[111]	31	*	75	77
	$[\bar{1}\,\bar{1}\,\bar{1}]$	38	22	*	*
TDE_ave		**45.2**	**41.09**	**50.45**	**45.0**
Carbon	[001]	19	18	*	54
	[110]	38	14	*	54
	[111]	31	16	*	90
	$[\bar{1}\,\bar{1}\,\bar{1}]$	58	*	*	*
TDE_ave		**35.6**	**15.45**	*	**60.54**

Table 3.9.1: Treshold diplacement energy values for this work compared with DFT analysis and experiment from [43], [44], [45]

It is clear that there is a wide difference of predicted values for 3C-SiC in the literature.

There have been several measurements of the E_d, with different techniques, but a large dispersion of values is obtained. In lack of precise data, Devianathan and Gao-Weber proposed as average values for the C and Si sublattices 20 eV and 35 eV, respectively (Atomic scale simulation of defect production in irradiated 3C-SiC**).** However, subsequent molecular dynamics studies did not clearly confirm these values. Average values were found from 17 to 40 eV for C sublattice and from 42 to 57 eV for Si sublattice, with extreme values very different.

The work of Lucas has shown that, in silicon carbide, the error due to the cell size problem is small compared to the discrepancy found between different calculation methods. This is an important point, because choosing for different box size does not interfere with the validity of this assumption.

3.9.1: Computational Method for TDE

For this work we took the threshold energy value from <100>, <110> ,<111>, and $< \bar{1}\,\bar{1}\,\bar{1} >$ directions using Erhart-Albe potential. In this section we describe the computational method.

The threshold displacement energy is determined by examining the response of a perfect crystal, when an initial kinetic energy is given to an atom located in the center of the simulation cell.

Consequently this atom, which is usually called the primary knock-on atom (PKA), recoils in the direction of the initial impulsion. The relaxation of the system is monitored and the amount of initial energy transferred to the atom is gradually increased (5 eV increment) until a stable Frenkel pair is formed, performing 10 runs for each threshold energy in order to increase the precision of our statistic.

In order to identify a stable Frenkel pair, we performed the Wigner-Seitz analysis over each of the 10 runs for each kinetic energy (1 eV increment).

Different results are expected for the Si sublattice as Si is heavier than C.

Indeed, higher energies are needed to create a stable Frenkel pair, which can be obtained with a secondary knock-on C atom in some cases. In our work, for Si [100] we found that the Frenkel pair forms at 34 eV, in good agreement with other MD simulations performed with Tersoff potential and in the same range of DFT. The Si [110] case is certainly the most complicated one due to the high kinetic energy transferred to the PKA. For example, Pearson [30] reported that Si PKA can form a defect for E_d = 146 eV.

However, in our work, defects formed at 31 eV, a low result compared to DFT data, but it is still in the same range of values for MD simulations data.

Along the Si <111> direction, we observed the creation of defects at E_d equal respectively to 36 and 38 eV.

The fastest way to visualize the stable defects formation is to plot the potential energy of the system in function of time for different kinetic energies of the PKA atoms as reported in Figure 3.9.3.

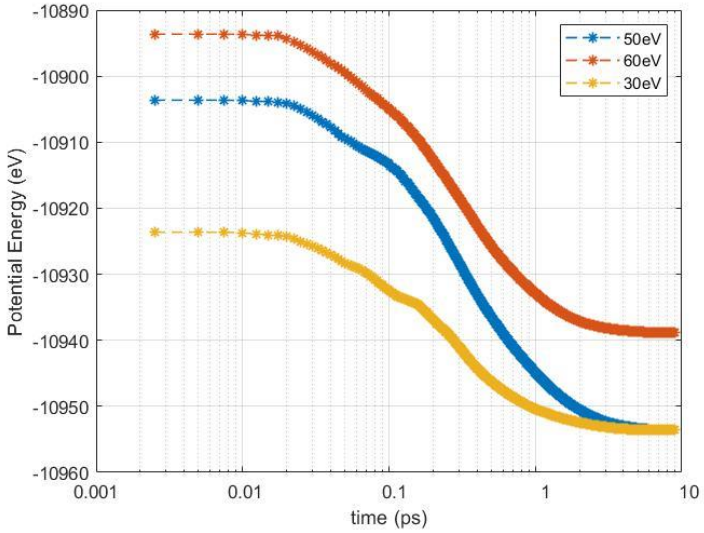

Figure 3.9.3: Potential energy of the system 3C-SiC in function of time for different kinetic energies of the PKA atoms.

In Figure 3.9.3, in yellow and blue we represented the potential energy tendencies in function of time for a TDE lower than the one necessary to produce a stable Frankel pair.

In fact the system ends at the same energy level. On the other hand, in red, it is represented the potential energy trend for TDE > E_d requested for a stable Frenkel pairs. On the third phase the system stabilized to higher value of energy because of the presence of defects which will not be annihilated. This method is easy and efficient, since it is not necessary to check for multiple value of energies opening every time Ovito analysis. In fact it was necessary to plot only the final value of the potential energy to visualize immediately the difference in energy between a intact system and the one with stable Frenkel pairs.

When the Si-PKA atom along <111> direction has a kinetic energy of 30 and 50 eV the vacancies and interstitials recombine and the system comes back to its original form. On the other end for E ≥ E_d (60 eV) the system relaxed to an higher value of potential energy.

3.10 NRT formulas to estimate damage creation

A simple procedure, the NRT formulation, is proposed for calculating the number of atomic displacements produced in a damage cascade by a primary knock-on atom of known energy. The formulae have been chosen to give results in close accord with recent computer simulations of radiation damage phenomena.
If we assume that the number of displacements produced by a PKA, n_{disp}, is proportional to the fraction of the PKA energy that is deposited in elastic collisions, T_d, we can write

For very low recoil energies E this number is given by

$$n_{displ,NRT} = 1 \qquad E_{TDE} < T_d < 2E_{TDE}$$

and for higher energies

$$n_{displ,NRT} = 0.8\frac{T_d}{2E_{TDE}} \qquad T_d > E_{TDE}$$

T_d is expressed in keV and is the total energy available for displacing atoms, excluding energy losses due to electronic excitation

E_{TDE} is the threshold displacement energy [31]:

The coefficient 0.8 can be seen as a kind of damage efficiency, originally deduced from binary collision approximation calculations [NRT], while E_{TDE} is the threshold displacement energy calculated for Si and C displacements.

In particular, it is possible to observe a certain number of displaced atoms only if $T_d > 2E_{TDE}$; otherwise, if $E_{TDE} < T_d < 2\ E_{TDE}$, only one atom is displaced from its original lattice site and there are no stable displacements at all when the damage energy of the incident neutron is lower than the threshold displacement energy.

The errors seen from NRT formula are related to the fact that it does not account for anything other than the total number of atomic displacements and it provides no information on in-cascade formation of point defects and clusters. Moreover, it has also been shown that at non-zero temperatures many of the created defects recombine, so that the net surviving defect fraction is even lower. This means that the dpa is mainly a conventional quantity to visualize the consequences of irradiation at 0K and to measure damage that allows comparison between different irradiation-induced changes of material properties and irradiation experiments with different particles (neutrons, ions, electrons, etc.).

3.11 Mathematical Development of NRT formula

In Norgett-Robinson-Torrens general formulation, T_d is expressed as following [32]

$$T_d = \frac{E_{recoil}}{1+k_d g(\epsilon_d)} \tag{3.32}$$

Where E_{recoil} is the energy of the recoil nucleus expressed in eV (in our case Si-PKA energy) and the other terms

$$\epsilon_d = \frac{a_L}{(Z_{rec}Z_m e^2)}\left(\frac{A_m}{A_m + A_{rec}}\right)E_{recoil} \tag{3.33}$$

$$a_L = \frac{0.88534 a_0}{\sqrt{Z_{rec}^{\frac{2}{3}} + Z_m^{\frac{2}{3}}}} \tag{3.34}$$

$$g(\epsilon_d) = \epsilon_d + 0.40244\epsilon_d^{3/4} + 3.4008\epsilon_d^{1/6} \tag{3.35}$$

$$k_d = \frac{0.0793\left(\left(Z_{rec}^{\frac{2}{3}} Z_m^{\frac{1}{2}}\right)(A_m + A_{rec})^{\frac{3}{2}}\right)}{A_{rec}^{\frac{3}{2}} A_m^{\frac{1}{2}}\left(Z_{rec}^{\frac{2}{3}} + Z_m^{\frac{2}{3}}\right)} \tag{3.36}$$

Where ϵ_d is the reduced energy accounting for the interaction between the atom of the medium and the recoil atomic particle. It comes for Lindhard (LSS) stopping theory [33]. It is calculated using the *Lindhard and Scharff screening length* a_L, a_0 is the Bohr radius expressed in A. $g(\epsilon_d)$, k_d and ϵ_d are dimensionless.

The Kinchin-Pease model, on the other hand, was modelled one year before the NRT formula (1975).

For Kinchin-Pease model the quantity Td stands for the energy available for damage production. For a single ion it is equal to the nuclear deposited energy $F_{d,n}$ = the total particle energy minus the energy that is lost to electronic stopping power:

$T_d = F_{d,n} = E_0 - F_{d,e}$.

The general formula looks almost the same as the NRT as we know it, but it is used the so called Firsov Model to calculate the total damage energy T_d [34].

The Firsov method consists in the distance of the closest approach.

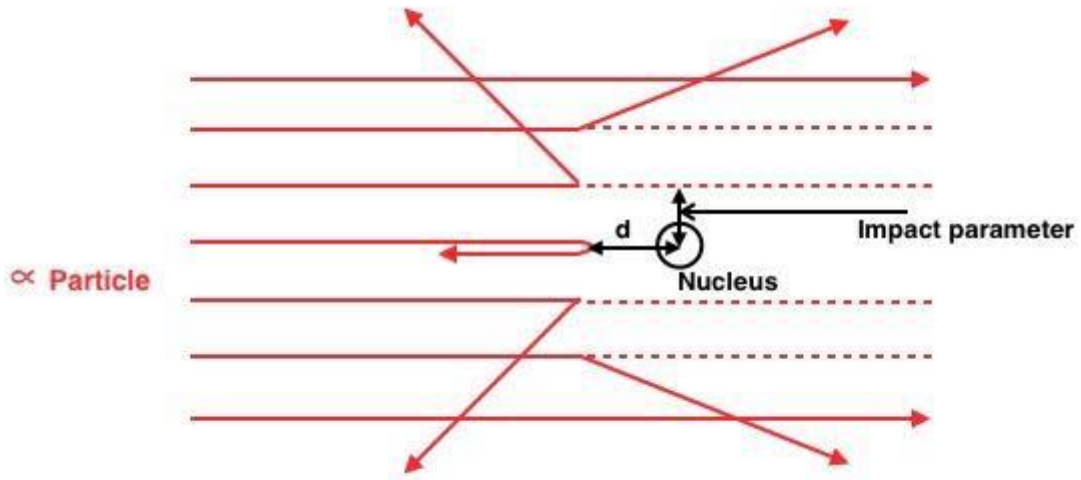

Figure 3.10.1: Distance of closest approach representation

When the ion travels directly towards the center of the nucleus experiences a large repulsive force and its velocity decreases and it reflects back.

The Distance of closest approach is the minimum distance between the recoil ion and the center of nucleus just before it reflects back by 180°.

Minimum distance of closet approach is given by

$$d_{min} = \frac{\frac{1}{4\pi\varepsilon_0}2Ze^2}{E_{recoil}} \tag{3.37}$$

In order to calculate the total damage energy it is necessary to calculate the total energy after the impact:

$$A = \frac{0.05941(Z_m Z_{recoil})^{\frac{5}{3}} E_{recoil}}{A_m} \tag{3.38}$$

$$B = 0.3042(Z_m Z_{recoil})^{\frac{1}{3}} \tag{3.39}$$

$$Q = energy\ loss = A/(1 + B \cdot d_{min})^5 \tag{3.40}$$

$$T_d = E_{recoil} - Q \tag{3.41}$$

As it is possible to see from the formalism, the model proposed the year before the NRT formula results more straight forward and simple to compute, giving similar results to computational methods as BCA methods (SRIM).

Chapter 4

4. Atomic structure of SiC and Graphite

This part of the thesis is dedicated to a brief analysis of the atomic structure of silicon carbide and graphite, pointing out on the description of all type of point defects present on SiC and graphite structure after irradiation.

4.1 SiC atomic structure

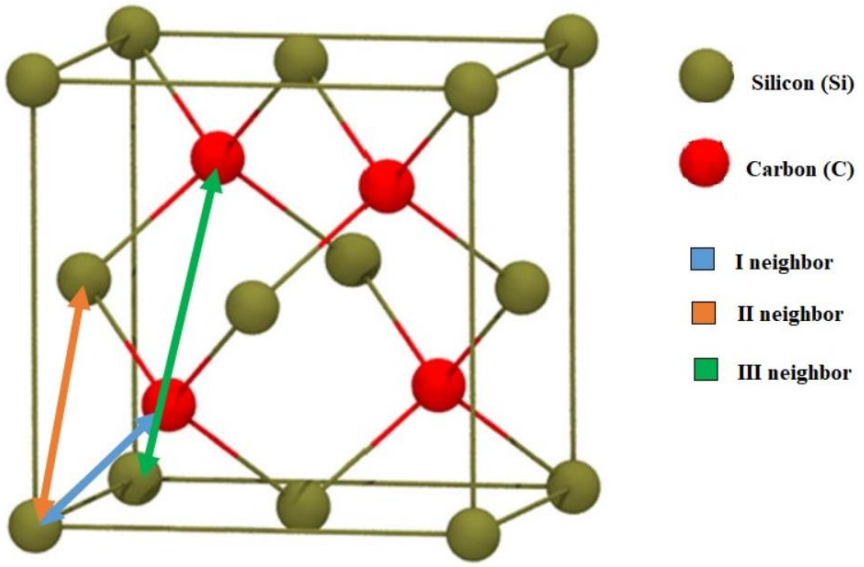

Figure 4.1.1: Schematic of a 3C-SiC unit cell. This structure is known as the `zinc-blende' structure. The red spheres are the carbon atoms, the larger ones the silicon. In blue, orange and green it is possible to distinguish the first, second and third neighbor distance in the cubic cell.

3C-SiC grows in zincblende structure, i.e. it is composed of two face-centered cubic (fcc) lattices, which are displaced by one quarter of the volume diagonal as in Si. However, in

3C-SiC, one of the fcc lattices is occupied by Si atoms while the other one is occupied by C atoms. Its lattice constant of 0.436 nm compared to 0.543 nm from that of Si structure and it results in a lattice mismatch of almost 20%, i.e. four lattice constants of Si approximately match five SiC lattice constants.

In SiC, a strong-bond oriented interaction allows creation of a stable structure if each atom has four nearest neighbors. The second neighbors are placed at distances which are 60 % greater when compared to the nearest neighbors. As a result, the amorphous phase is very close in energy to the crystalline one and it's very easy to create metastable interstitial-vacancy pairs with a sizable recombination barrier [24]. Generally the total number of clusters is such that the typical distance between nearest neighbor vacancies has no more incidence than the second nearest neighbor distance for the lattice structure. As cut off distance has been chosen 3.8 Å, a quantity between the third and the fourth nearest neighbor ($\sqrt{\frac{11}{4}\cdot a}$ and and $\sqrt{\frac{19}{4}\cdot a}$). This value is taken to mean that it contains a sufficient number of vacancies and interstitials to form a stable geometry and does not change shape or size drastically by very short term (few picoseconds or less).

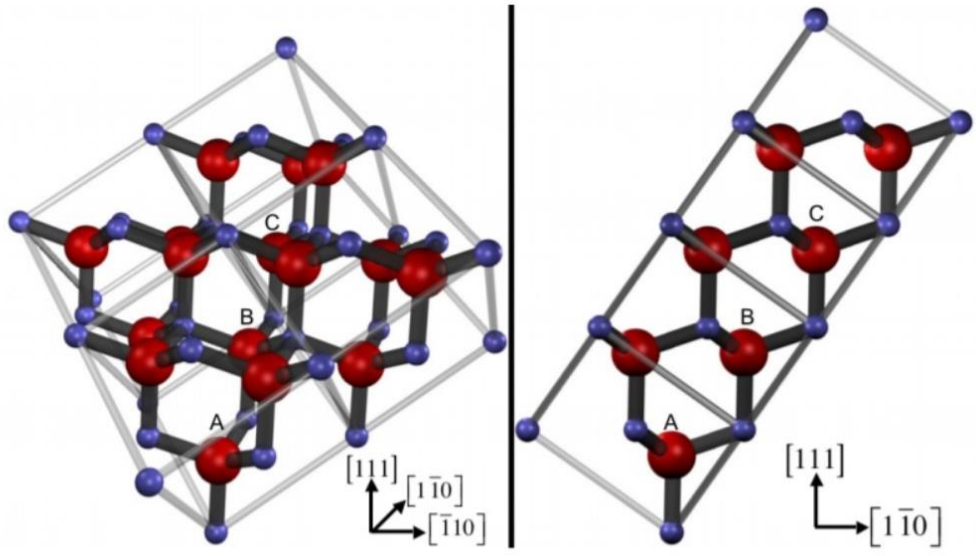

Figure 4.1.2: Schematic representation of the stacking order of 3C-SiC (cubic stacking). 3C-SiC is one of the extremes of the SiC polytypes, and is the only cubic polytype. Miller indices are given to show the orientation, the large and small spheres in each bi-layer denote a silicon and carbon atom, respectively [35].

4.2 Graphite atomic structure

The two types of atomic sites found in graphite can be categorized as those situated between immediate neighbors above and below and those with open hexagons immediately above and below.

Graphite in a highly perfect crystalline form, shows a planar morphology with a silvery surface. Graphite is extremely soft and can be deformed easily.

To build the unit cell of the graphite we used the following orthogonal representation to defined the coordinates of each carbon for the α and β layer.

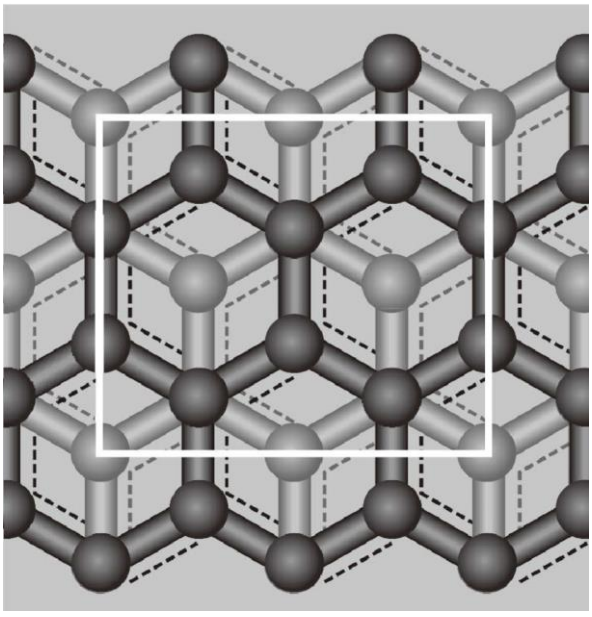

Figure 4.2.1: An orthogonal unit cell (white solid lines) viewed from the top for graphite. The carbons (circles) in the A (B) planes are shown in dark (light) gray circles [36].

In the unit cell there are respectively 4 atoms of α layer and 4 of β layer.

4.3 Point defects

The main crystallographic point defects that we can find in an irradiated SiC and graphite are:

- *Vacancies (both point defects and clusters)*. Lattice sites which would be normally occupied in a perfect crystal, but are vacant;

4.3.1 SiC: vacancies

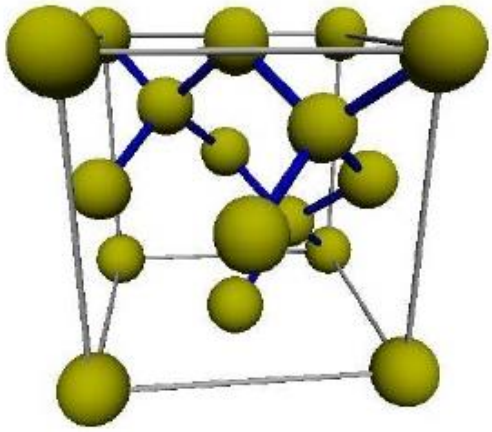

Figure 4.3.1: Si vacancy 3D representation [37]

In 3C–SiC, there are two types of vacancies, namely the C and Si vacancies with four Si or four C atoms as nearest neighbors, respectively. In DFT calculation reported in literature ([22],[41],[42]) the V(C) results the one with lower formation energy than V(Si).

4.3.2 Graphite: vacancies

On the other hand, for graphite, we only find V(C).

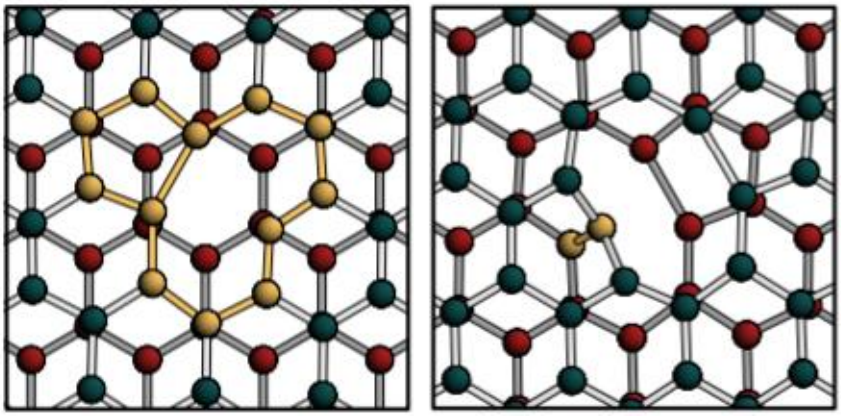

Figure 4.3.2: β-vacancy in graphite (coplanar class) and cross-layer $V^{\alpha\beta}$ vacancy (cross-layer class) 2D representation [38]

The vacancies found in graphite after relaxation are divided in classes: coplanar and cross-layer. The first class be regarded as being 'close', in the sense that they have significant binding energy, and are not more than third-neighbor separation.

- *Self-interstitial atoms (SIA) and clusters*. Atoms of the same type as those already present in the lattice which occupy a site in the crystal structure where there is usually not an atom, or two or more atoms sharing one or more lattice sites such that the number of atoms is larger than the number of lattice sites;

4.3.3 SiC: interstitials

While only 2 vacancies exist in SiC, the available interstitials are numerous. The most important configuration are defined in the picture below.

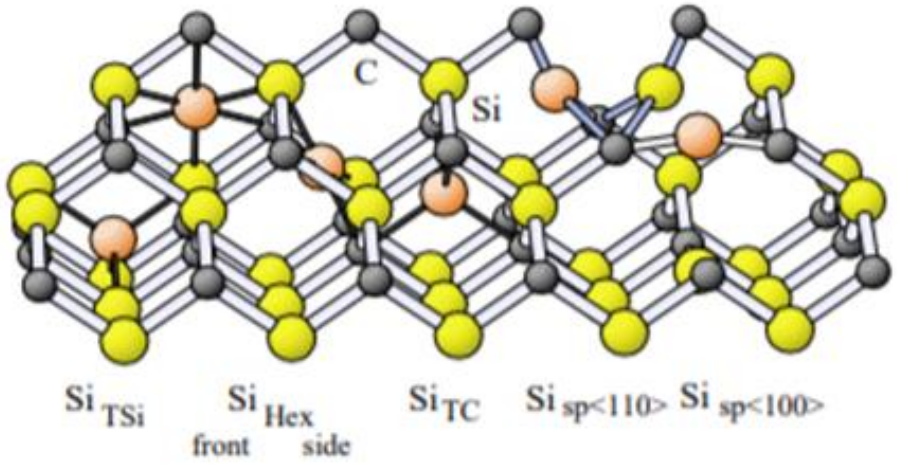

Figure 4.3.3: Configurations of Si interstitials in SiC (in yellow Si and in grey C atoms). Interstitials Si atoms are represented as orange spheres [39].

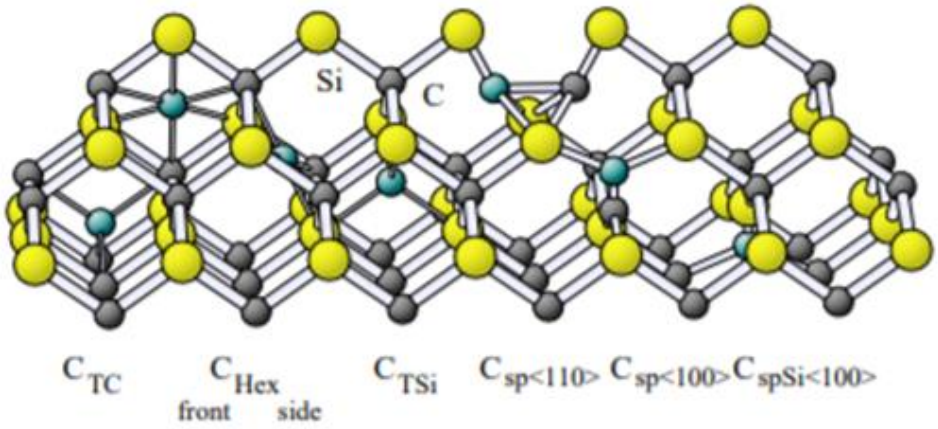

Figure 4.3.4: Configurations of C interstitials in SiC (in yellow Si and in grey C atoms). Interstitials C atoms are represented as green spheres [39].

Some of the defects are only distinguished by their environment like the tetrahedrally coordinated interstitial sites, which either possesses a silicon-like (I_{TSI}) or a carbon-like (I_{TC}) surrounding.

These tetrahedral interstitials can be categorized as Si tetrahedral interstitials and C tetrahedral interstitials. The former can be classified by two types: an empty tetrahedral interstitial framed only by four Si atoms (Tsi for short) and a filled tetrahedral interstitial also framed by four Si atoms but with a C atom in the center (T_{Si_C}). Similarly, the latter

also has a hollow tetrahedral interstitial by C atoms (Tc) and a filled tetrahedral interstitial with a Si in the center (T_{C_Si}). These tetrahedral interstitial configurations, just like cages, are represented in the Figure 4.3.3 and Figure 4.3.4 [40].

Another important site is the Hexagonal configuration $I_{HEX,}$ which is located in the center of an hexagon of alternated Si and carbon atoms.

Another distinct interstitial is the split-interstitial I_{sp}. In this configuration, the interstitial atoms share sites with a lattice atom of either type. Of these dumbbell-like defects, the $C_{<100>}$ is the most observed one.

4.3.4 Graphite: interstitials

Isolated, single self-interstitial atoms are predicted by DFT to exist in four distinct forms: spiro, grafted, α-split, and β-split, defined previously in literature Heggie and Latham [38]. In Matlab we built manually the same interstitial structures].

The spiro state comprises four nearest neighboring atoms from the host, two in each of two adjacent layers, plus the interstitial atom near their center of mass, with six bonds linking the five atoms. On the other hand, Y-lid transition is characterized by a Y shape bond between α and β graphite layers.

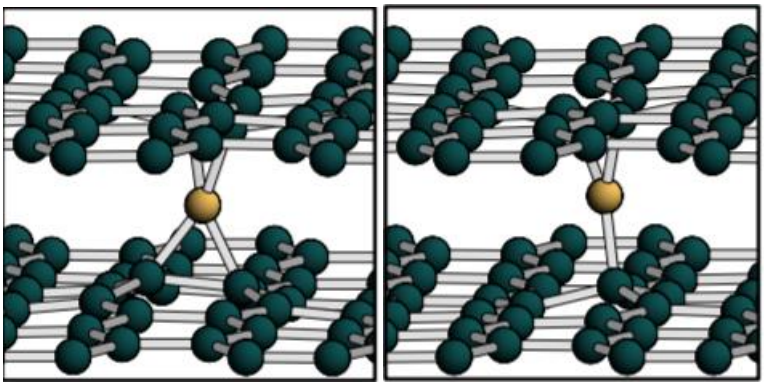

Figure 4.3.5: Interstitial atoms in graphite: the spiro interstitial and Y-lid transition state. The prismatic types of interstitials have been seen to be, in literature, the most unstable forms, changing shape, directions and bonding after relaxation [38].

Grafted interstitial atoms form a triangular structure bridging the bond between two neighboring atoms in the same graphene sheet of the host as represented in the figure below.

This type of defects doesn't occur only in the bulk of the material, can be also observed on the surface of graphite.

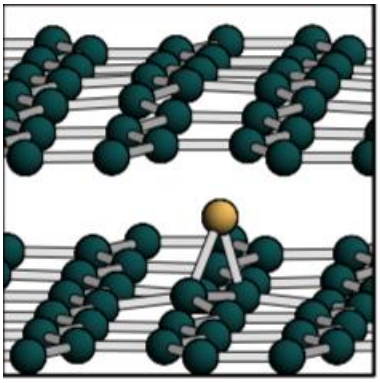

Figure 4.3.6: Grafted interstitial defect in graphite [38]

Since the spiro is one of the most unstable type of interstitials, to reach a neighboring pair of α atoms, a migrating interstitial atom must first escape from the spiro state to a neighboring grafted state, then move to a split-interstitial on a β-site, followed by the next neighboring grafted state, before reaching a new spiro state.

The two types of split-interstitial have a pair of carbon atoms sharing an α or β site in a graphite crystal, with the bond between the pair aligned in the prismatic direction as represented in the figure below.

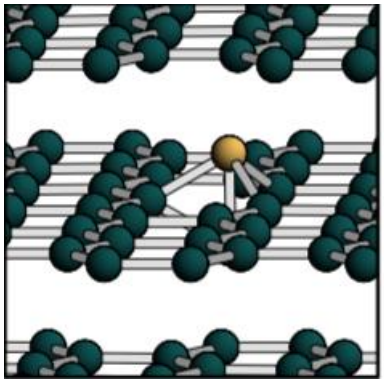

Figure 4.3.7: β-split interstitial defect in graphite [38]

Finally, the canted-interstitial can represent a partial substitute for a true spiro-interstitial structure. In this case, two bonds combines the carbon atoms on two subsequent layers.

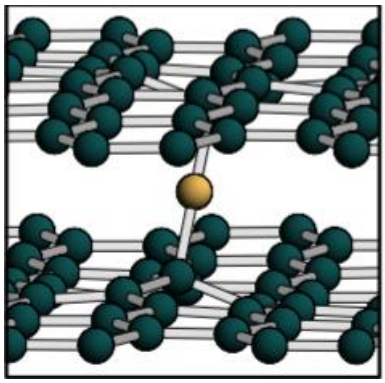

Figure 4.3.8: Canted interstitial defect in graphite [38]

- *Antisites*. This defects occur in an ordered compound when atoms of different type exchange positions. For example, some compounds have a regular structure in which every other atom is a different species; for illustration assume that type A atoms sit on a certain position, and type B atoms sit in in a different one. When during irradiation an A atom moves from its position to a site normally occupied by a B atom it is thus an antisite defect. This is neither a vacancy nor an interstitial, nor an impurity. This type of defects are present in compounds with more than one type of atoms (no graphite).

-*Frenkel pairs*. This defect represents a type of 'point defect' in a crystal structure where an atom is displaced from its normal position to an interstitial one, leaving a vacancy behind.

Chapter 5

5. Results and Discussion

This part of the thesis is devoted to an analysis of the results obatained through computational methods in MD and BCA.
The results obatained have been analyzed and manipulated in Matlab in order to have a visual analysis of the data.

5.1 Potential Selection

5.1.1 SiC potentials

A total of 10 potentials have been used to compare the lattice parameter and the cohesive energy of a SiC supercell.
Tersoff potentials can be applied on silicon, carbon and also to multicomponent systems like silicon carbide.
The Gao-Weber potential has been taken into account as an empirical many-body interatomic potential. It is developed by fitting to various equilibrium properties and stable defect configurations in bulk SiC, using a lattice relaxation fitting approach. In the end, it has been excluded because it cannot correctly reproduce the C-C interaction in graphite. From literature, in fact, the Gao–Weber potential provides a satisfactory description of SiC properties, but it has been excluded for its incompatibility with C-C bonds in pure graphite.
A compilation of data in Table 5.1.1 includes results obtained with our SiC potential and with three different versions of the Tersoff potential [T89, T90, T94, Erhart-Albe] for SiC and by Gao and Weber's. Obviously, the SiC parametrization of EH05 bond-order potential

reproduces all cohesive energies and lattice constant very well, especially in comparison to experimental and DFT data.

	Exp.	DFT	TERSOFF	TERSOFF_89	TERSOFF_90	TERSOFF_94
	3C-SiC	3C-SiC	3C-SiC	3C-SiC	3C-SiC	3C-SiC
***a* (Å)**	4.36	4.34	4.32	4.32	4.31	4.28
| *Ec* (eV/Å)	-6.34	-7.42	-6.16	-6.16	-6.21	-6.43

	ERHART-ALBE	GAO-WEBER	TERSOFF/ZBL	GAO-WEBER/ZBL	EDIP	MEAM
	3C-SiC	3C-SiC	3C-SiC	3C-SiC	3C-SiC	3C-SiC
***a* (Å)**	4.36	4.36	4.28	4.36	4.36	4.36
| *Ec* (eV/Å)	6.34	-6.41	-6.43	-6.41	-6.34	-6.43

Table 5.1.1: results of lattice parameter (a) and cohesive energy (E_c) obtained using different potential formalism

A tetrahedrically coordinated carbon interstitial can be surrounded either by four carbon (C_{TC}) or four silicon atoms (Si_{TC}) and equivalently for Si (respectively Si_{TSi} and C_{TSi}). For dumbbell two configurations have been considered for this study: C-$C_{<100>}$, C-$C_{<110>}$, Si-$Si_{<100>}$ and Si-$Si_{<110>}$.

In Table 2 the different formation energies have been listed compared to DFT results obtained by the available literature on point defects in silicon carbide structure.

	DFT				TERSOFF	TERSOFF_89	TERSOFF_94	ERHART-ALBE	EDIP
VACANCIES									
	[22]	[22]	[41]	[42]					
V_C	4.5	4.2	3.63	4.46	0.39	0.39	6.09	1.81	1.55
V_{SI}	8.2	8.1	7.48	6.04	6.64	6.64	5.91	4.65	4.28
ANTISITES									
C_{SI}	3.8	3.4	3.48	0.47	2.22	2.22	0.37	2.18	2.38
SI_C	4.6		4.02	9.49	4.26	4.33	8.03	2.25	2.72
CARBON INTERSTITIALS									
C_{TC}	12.4	-	6.31	5.95	7.18	7.18	6.52	12.69	7.89
C_{TSI}	10.0	-	6.31	6.37	4.38	4.38	3.44	9.40	6.39
$CC_{<100>}$	-	-	6.31	5.91	6.10	6.37	10.08	5.07	4.82
$CC_{<110>}$	-	-	-	-	7.88	7.88	6.93	10.63	5.90
SILICON INTERSTITIALS									
SI_{TC}	13.3	-	7.04	7.65	17.48	17.48	18.72	17.38	12.97
SI_{TSI}	13.6	-	9.23	7.84	15.30	16.11	19.34	18.09	12.34
$SISI_{<100>}$	-	-	9.32	-	14.68	14.67	18.29	17.71	8.3
$SISI_{<110>}$	-	-	8.11	-	15.78	15.78	18.78	18.08	9.3

Table 5.1.2: results of points defect formation energies obtained using different potential formalism

One of the main objectives of this work was an analysis of the point defects description in silicon carbide compared to existing classical potentials. Here, one shows the results obtained for the cubic phase.

The method chosen to identify the most stable configuration consists in comparing the formation energy obtained using the empirical potentials with those obtained with DFT calculations. In fact, the most stable configuration corresponds to the lowest value derived from DFT results. In the same way, comparing the different values obtained with empirical potential, we have chosen the one that follows the same logic used for DFT.

Considering first the vacancies, the formation energies for carbon vacancies computed with all potentials apart the new version of Tersoff (T94) are smaller than those found for silicon vacancies as defined by the DFT results.

The most stable configurations is found in literature to be $CC_{<100>}$ dumbbell interstitial. The tetrahedral interstitials, on the other hand, are found to be significantly higher in energy. All Tersoff potentials, apart EA05, yield formation energies of dumbbell interstitials higher than for other types of interstitials showing that C_{TSi} tetrahedral configurations are the most stable defects, contradicting the results found in DFT. So, only EA05 and EDIP are in accordance with the predictions of DFT analysis provided in the table. The properties of silicon interstitials are very difficult to reproduce with empirical potentials. DFT calculations showed that the most stable configuration is the Si_{TC} tetrahedral interstitial. From this last results, it is possible to exclude EDIP potential, since it predicts that $SiSi_{<100>}$ dumbbell is the most stable configuration, incompatible with the results obtained in DFT. Therefore, our final choice fell on EA05 potential.

5.1.2 Graphite potentials

For the first part of this work one is interested in choosing the suited potential for atomic scale simulations of processes which involve transitions between widely different atomic configurations. In the course of the this first set of data it has been derived parameters for both Si-C interactions for both silicon and carbon and revisited the parameters set for C-C bonds too.

For graphite 6 potentials have been chosen.

The database for fitting procedure includes experimental data such as cohesive energy and lattice parameter of Si, C and SiC which ensure that the potential and DFT calculations will accurately reproduce the structural and elastic properties of the materials.

Bulk carbon

Graphite sheets are held together by long range Van der Waals interactions, a typical feature which is difficult to reproduce with short-range classical potentials (EAM and ZBL potentials control the atomistic dynamics at low distances). As shown in Table 5.1.3 Tersoff, T89 and EDIP potentials reproduce reasonably well the cohesive energy of the structure. Unlike other potentials, EDIP tends to slightly overestimate the lattice parameter of graphite. On the other hand the best agreement between DFT and potential calculation of both lattice parameter and cohesive energy is obtained by the Erhart-Albe (EA05) potential.

	Exp.	**DFT**	**TERSOFF**	**TERSOFF_89**
	Graphite	Graphite	Graphite	Graphite
***a* (Å)**	2.46	2.44	2.53	2.53
E_c **(eV/Å)**	-7.374	-9.03	-6.16	-7.39

	TERSOFF_90	**TERSOFF_94**	**ERHART-ALBE**	**EDIP**
	Graphite	Graphite	Graphite	Graphite
***a* (Å)**	2,69	2,74	2,56	2,59
E_c **(eV/Å)**	-5.31	-5.31	-7.37	-7.38

Table 5.1.3: Results of lattice parameter (a) and cohesive energy (E_c) obtained using different potential formalism

There are a variety of empirical interatomic potentials for carbon, the most commonly used are those developed by Tersoff and Brenner (commonly known as AIREBO or REBO). Generally it can be possible that some inconsistencies are present between the results found through the empirical potential and the DFT calculations (GGA,LDA…)

A total of 4 simple defects (**see Chapter 4.3.5**) have been included in the study of graphite interstitials. Isolated, single, self-interstitial atoms are predicted by DFT to exist in four distinct forms: spiro, grafted, α- and β-split. The two types of split interstitials have a pair

of carbon atoms sharing and α and β site in a graphite crystal, with the bond between the pair aligned in the prismatic direction.

The spiro state comprises four nearest neighboring atoms from the host, two in each of two adjacent layers, plus the interstitial atom near their center of mass.

The results of the calculation are summarized in the following table where it can be see that the extent to which the two Tersoff potential (Tersoff and Erhart-Albe (EA05)) and the EDIP potential are able to reproduce the DFT structures and energies is in most cases at least qualitatively acceptable.

	DFT				TERSOFF	ERHART-ALBE	EDIP
VACANCIES							
	[43]	[43]	[44]				
V_{CB}	-	8	7.8		7.50	5.88	6.88
V_{CA}	7.6	-	-		7.50	5.88	6.88
CARBON INTERSTITIALS							
	[45]	[46]	[44]	[44]			
SPIRO	5.85	6.3	6.5	6.9	4.40	3.11	3.04
GRAFTED	7.55	7.78	7.8	8.4	8.80	8.42	4.21
A-SPLIT	7.12	7.27	-	-	11.56	11.65	6.14
B-SPLIT	7.23	7.36	7.3	-	11.56	11.65	6.14

Table 5.1.4: Results of points defect formation energies obtained using different potential formalism

5.1.3 Conclusions:

Following the same method we used for graphite, also in this case the results found using the EA05 potential agree with those proposed in literature using DFT analysis. Spiro is, accordingly to DFT analysis, the most stable defect, such as EA05 predicted. In conclusion

we defined that the chosen potential for our calculations would have been the empirical potential developed by Erhart-Albe (Tersoff many-body type) in 2005.

5.2. Stopping power in SiC

Generally, in the MD method, the energy loss of the ion is calculated by using many-body-interactions and the information of the local electron environment. Thus it is more accurate in predicting the range profiles for low energies. In particular, energy losses affect the total atomic displacements especially in high energy cascades as it is possible to see in the figures below, where electronic and nuclear stopping power have been reported in function of Si and C PKA energy.

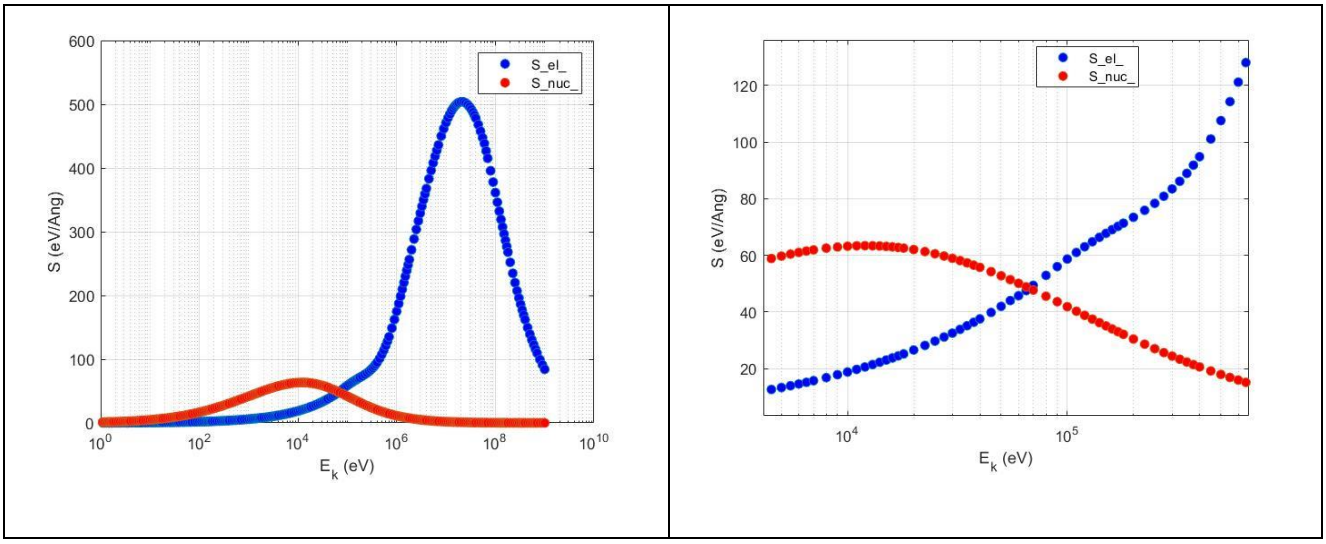

Figure 5.2.1: Electronic and nuclear stopping power for Si-PKA atom in function of PKA kinetic energy. On right-hand picture it is represented the evolution of the electronic and nuclear stopping power for 1keV < E_k <100 keV.

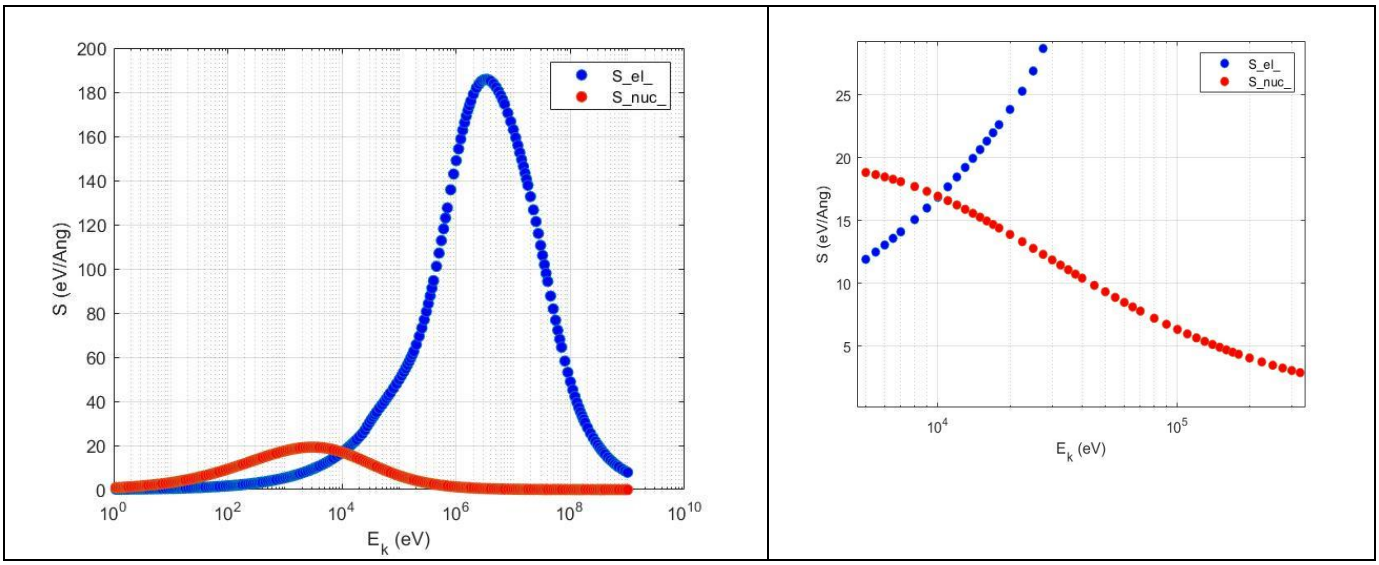

Figure 5.2.2: Electronic and nuclear stopping power for C-PKA atom in function of PKA kinetic energy. On right-hand picture it is represented the evolution of the electronic and nuclear stopping power for 1keV < E_k <100 keV.

The main effect of the coupling between electronic and ionic subsystems during the ballistic phase of the cascade is the electronic stopping ES of energetic recoils, which is fairly well understood and motivated both experimentally and theoretically for higher energies.

The contribution of the electronic stopping power is incorporated into MD simulations as a frictional force on moving atom.

Furthermore, the SRIM stopping power is extrapolated down to zero kinetic energy and it has been found a linear correlation between the velocity of the incoming ion and its kinetic energy for both Si and C PKA.

In order to incorporate the electronic stopping power in MD simulation, we have to calculate the friction term which modifies the velocity of all the particles in the system. In this case, it is necessary to calculate the velocity of the incoming particle.

The velocity calculated in function of the kinetic energy follows the Newtonian mechanics (conservation of energy)

$$v = \sqrt{2 \cdot E_k / A} \tag{5.1}$$

Where E_k is the kinetic energy of the incoming particle and A is the atomic mass of the particle (C=12 amu and Si=14 amu).

We fitted the results obtained for C and Si PKA particles in the following pictures.

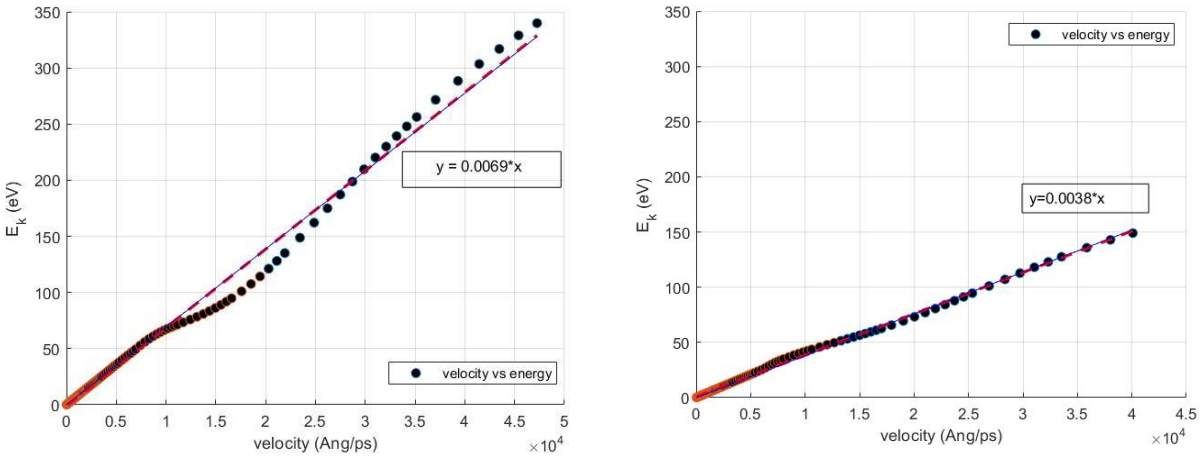

Figure 5.2.3: A) Velocity of the Si-PKA atom in Ang/ps in function of the kinetic energy. As it is possible to see from the picture the tendency of the curve can be approximated with a linear regression as y=0.0069·x.

B) *Velocity of the C-PKA atom in Ang/ps in function of the kinetic energy. As it is possible to see from the picture the tendency of the curve can be approximated with a linear regression as y=0.0038·x.*

For the current analysis we chose the analytical bond-order potential (BOP) developed by Albe et al. Point defects properties and lattice parameters have been found in good agreement with what reported in literature. Furthermore, the Tersoff-Brenner parametrization developed by Alber et al. was validated on ab initio calculations for multiple defect type calculations **(see Chapter 5.1.1).**

However in order to simulate the interaction of high energy Si-particle with SiC, the short range interactions have been further modified to match the screening function ZBL potential that gives a good representation of high energy scattering of atoms in solids. This is achieved by coupling the original BOP and the short-range function through the use of the Fermi function.

The total potential is dominated by the ZBL profile for a short distance and quickly approaches the BOP as r increases. A_F and r_C are defined in order to make the ZBL potential fitting the Erhart-Albe trend. We identified A_F with 28 A^{-1} and r_C with 0.95 A for Si-C interactions.

It is clear that as the PKA energy increases, the projectile is then able to overcome the BOP repulsion interactions, which are captured by the ZBL potential. For very high PKA energies, the pair distance becomes very small, leading to a big increase of the atomic forces extended between the pairs. So the ZBL potential becomes the dominating functional, enabled by the Fermi equation where the BOP defines interactions for longer ranges.

In order use the stiffened Erhart-Albe potential we re-calculated the defect formation energy again, in order to see that for the ZBL version of the potential the values remained unvaried. In fact, all the results have been confirmed from the reevaluation of formation energy.

5.3 Cascades in SiC

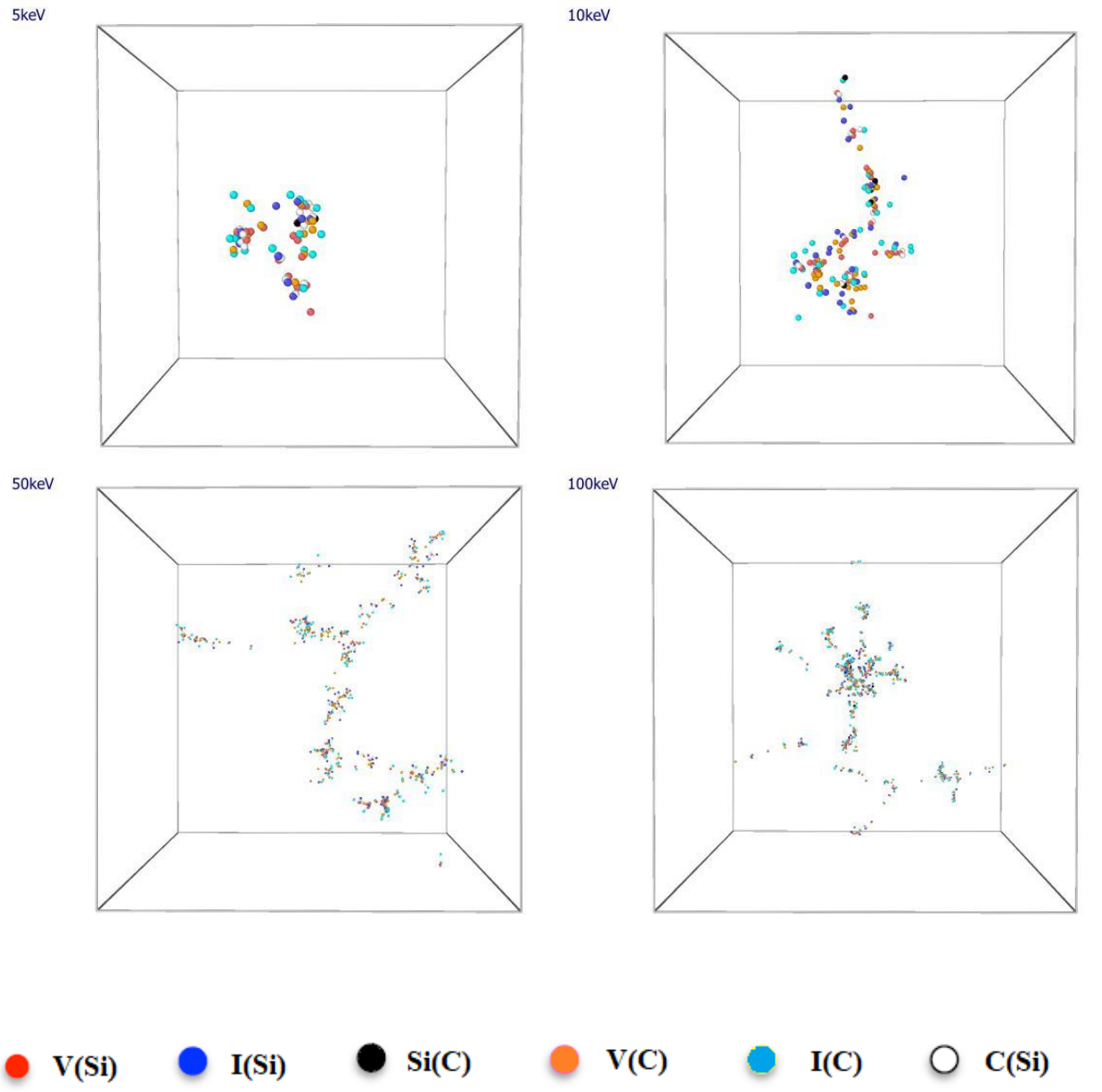

Figure 5.3.1: The final defect states of at 5keV (a), at 10 keV (b) and a 50 keV (c) and 100 keV (d) cascade in SiC from which can be clearly seen the transition from a single pocket of atomic displacements to multiple subcascades.

The figure shows the final defect distributions and cascade morphologies produced by 5, 10, 50 and 100 keV cascades in SiC. The defects generated by a PKA with an energy less than 5 keV distribute on one cascade region, and consist of interstitials and vacancies, rather than antisite defects. However, a PKA generates multiple sub-branches of the cascade along

its path when its energy is larger than 5 keV, which is clearly displayed in the last three blocks, forming distinct regions separated from each other with a high energy density in the cores of the sub-branches.

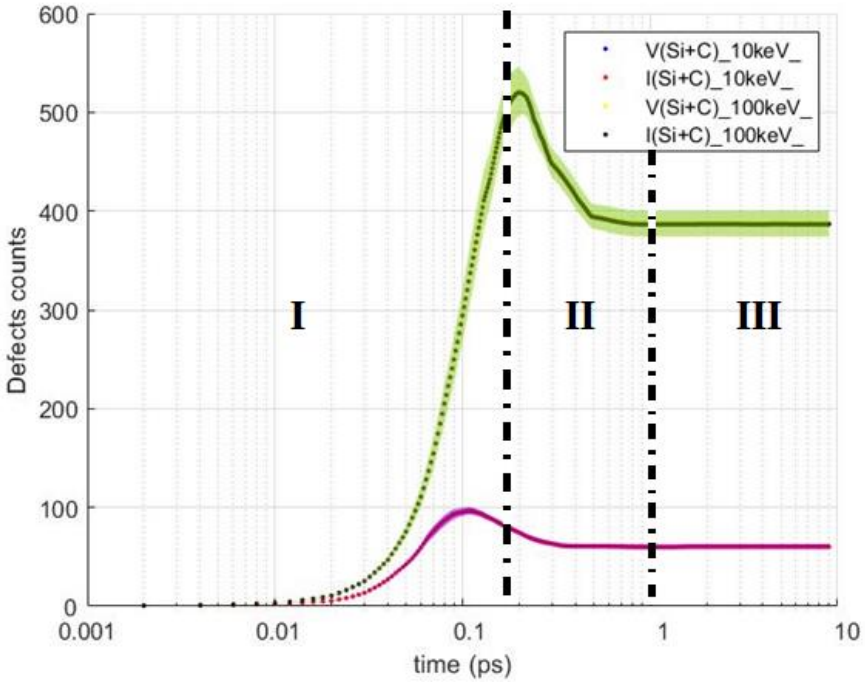

Figure 5.3.2: Plot of the total number of vacancies or interstitials (C defects plus Si defects) for 10 keV ans 100keV Si-PKA through the simulated time.

In the course of the point defect identification, the number of each type of point defect at each output step was tabulated. The defect counts at each output step for all of the 10 (non-overlap via periodic boundaries) runs were then averaged, tabulated and plotted with their standard error. This indicates that all of the displaced atoms have been accounted for in the defect identification stage, as no atoms were gained or lost during the simulation. The specific point defects tabulated were vacancies, interstitials, antisites and replacements for both Si and C. In the previous image it is represented the sum of C and Si vacancies and the sum of C and Si interstitials showing that the total number of those two type of defects is conserved, proving that the simulation worked correctly. It also indicates the general trend that is expected is respected. The maximum number of defects were created in the initial collision phase (I), and reached a final 'stable' number in phase III, the cooling phase.

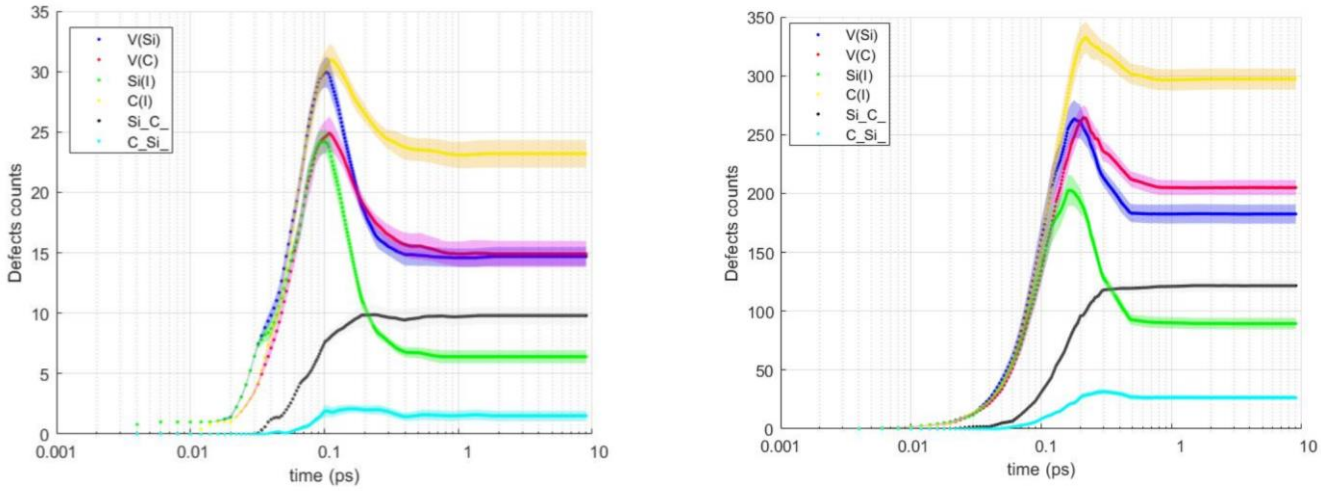

Figure 5.3.3: Plots of the number of Si and C defects averaged over the 10 non-wrap-around runs and different energy Si-PKA values (5keV, 100 keV).

From the Wigner-Seitz analysis performed in Ovito, it was possible to determine the evolution of defects formation in function of time (ps). This gives an idea on what type of defects are more persistent in the system.

In the course of the point defect identification, the number of each type of point defect at each output step was tabulated. The defect counts at each output step for all of the 10 independent runs were then averaged, tabulated and plotted. The specific point defects tabulated were vacancies, interstitials, antisites and replacements for both Si and C. The plots of the number of interstitials and vacancies are shown in the previous figures. Defects count for 2 values of energy have been represented: 5KeV and 100 keV. Furthermore it is possible to see that for very low energy the C and Si vacancy counts are approximately the same during the III phase (cooling down phase), while C vacancies results in majority (200 V(C) vs 175 V(Si)) for PKA energy of 100 keV. Both the figures illustrate the number of interstitials and antisite defects formed in the system.

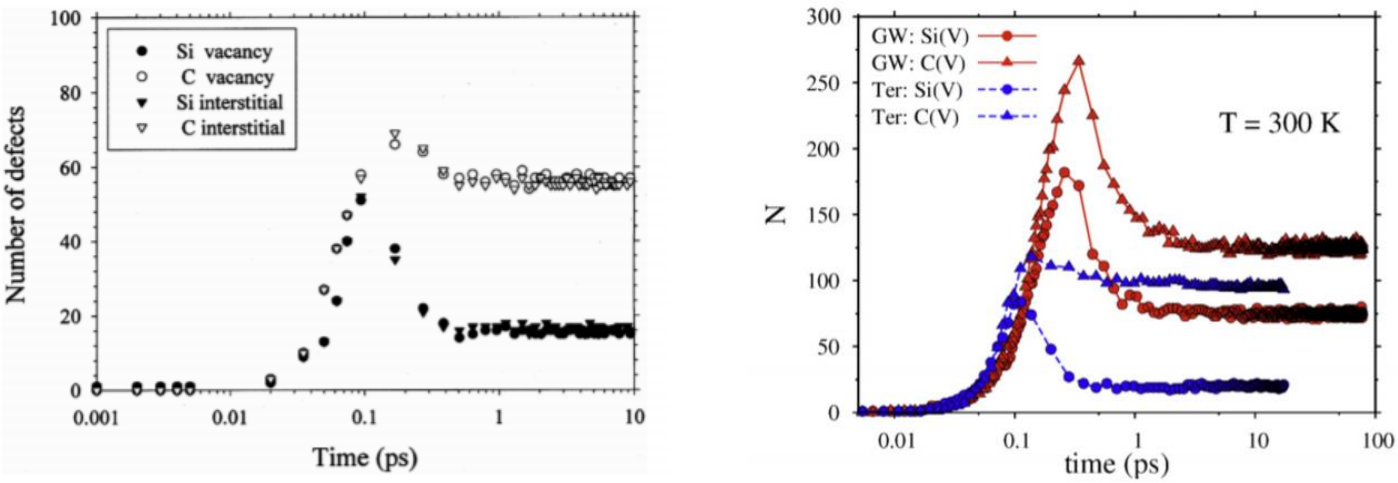

Figure 5.3.4: Plot of the number of C and Si vacancies created by 10 keV Si-PKA in function of time simulated in this work from Devanathan and Samolyuk [47]*[24] . The two plots differs from the one of this work because the temperature was controlled during the simulation by coupling the atoms along the four cell boundaries to a reservoir of heat at 300 K while the simulation of this work has been kept at 0 K.*

As is possible to see from all the three plots, the qualitative shape of the evolution is the same, with the peak values at roughly the same time. The biggest difference that is possible to observe is the ratio C:Si vacancies. While in this work a frictional contribution has been considered, the number of Si and C vacancies has nearly a 1.5:1 C:Si vacancy ratio compared to the significantly higher 3:1 ratio reported by Devanathan and 2:1 C:Si ratio and 4:1 C:Si ratio reported by Samolyuk using respectively GW and T89 empirical potentials.

A C_{Si} antisite defect is when a C atom fills what initially was an Si site and a Si_C antisite defect is when a Si atom fills what was a C site. It can be determined that the total number of 'stable' replacements and antisites (Si(C), roughly 125 for 100keV Si-PKA) is almost 25 % higher than the number of interstitials (roughly 100 for the same conditions). It is also evident that SiC antisite formation occurs more frequently than CSi antisite defect formation and Si replacements. Further, it appears that the majority of the antisites formed are stable for the timescale studied in these calculations. The only decrease occurs in the

CSi antisites, where less than 10% reduction after the initial collision phase is seen. The existence of so many antisites also has the implication that one may find small localized regions of Si or C that have not necessarily formed into distinct 'inclusions' nor become a locally amorphous structure [48]. As expected from literature, the C(I) are those defects with the lowest formation energy. In fact, the number of stable C(I) defects results the highest for both 5 keV and 100 keV Si-PKA (25 for 5keV and 300 for 100keV).

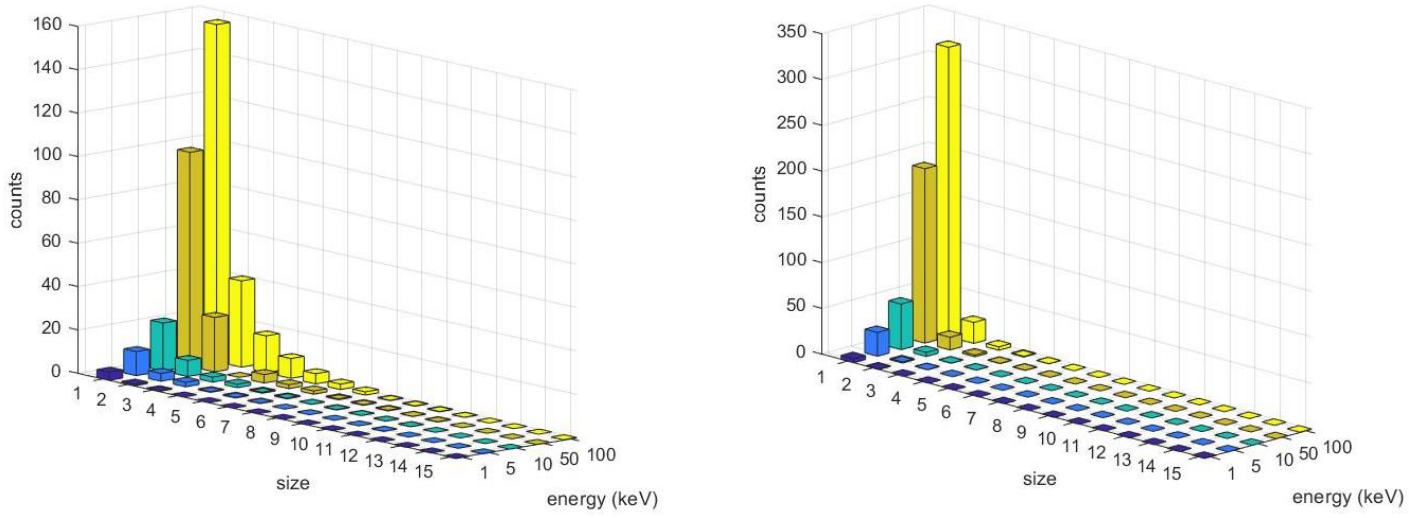

Figure 5.3.5: A) The graph represents a statistics of vacancy cluster count versus the cluster size. The five group of columns represent the values found for 1keV, 5keV, 10keV, 50keV and 100 keV. B) The graph represents a statistics of interstitial clusters count versus the cluster size. The five group of columns represent the values found for 1keV, 5keV, 10keV, 50keV and 100 keV.

As shown in the two figures above, clusters have been grouped depending on energy and size. For both interstitials and vacancy clusters it is possible to notice that for each Si-PKA energy the cluster size goes from 1 to larger sizes following a power law.

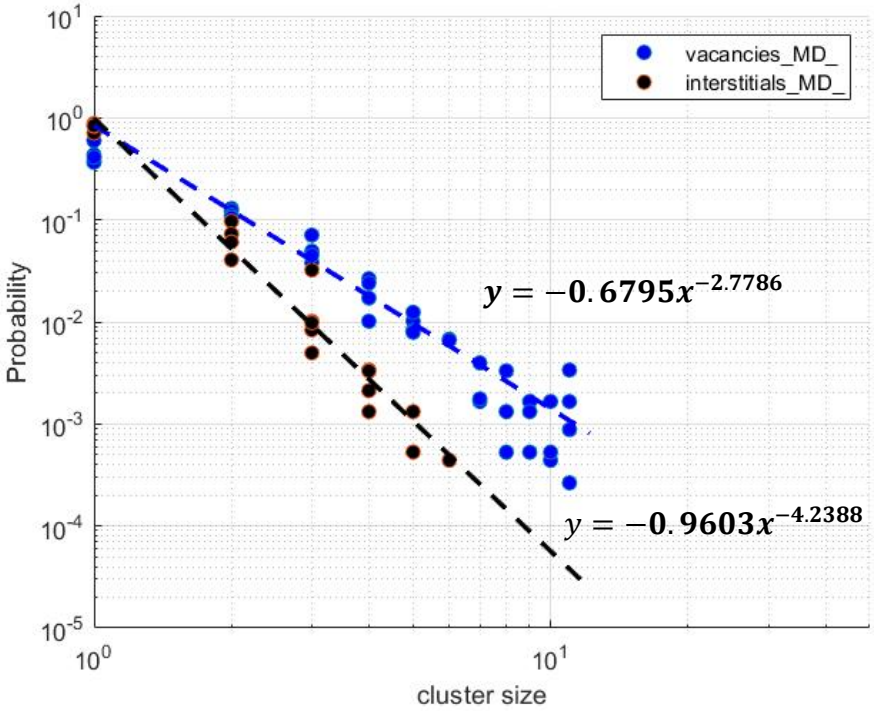

Figure 5.3.6: Interstitial and vacancy clusters linear approximation in function of the cluster size. In the picture is possible to see that bot interstitial and vacancy clusters follow a linear approximation on logarithmic scale.

In the figure above it is possible to see the linear regression of the probability of insertion of clusters in SiC for various Si-PKA energy in function of the size.

The clusters inside the bulk of SiC have been sorted by size and energy. In order to compute the power law presented in the graph above we normalized the clusters of each size as

$$P_i = \frac{cluster_i}{N_{cluster,tot}} \quad i = 1,2,3.. \tag{5.2}$$

P is ratio between the clusters of each size and the total number of clusters for each PKA-energy, so the probability of clusters of each size to exist.

Finally, we showed that the probability distribution function of the clusters in a system doesn't depend on the energy of the incoming particle, but only on the cluster size as shown

in the plot. Both vacancy and interstitial clusters probability can be approximated through a power law of the type

$$y = bx^{-m}$$

as shown in the graph.

The power law found from the MD simulations is the beginning of the enhancement of the defect calculations in SiC. Using faster methods as BCA based programs will reduce significantly the computational cost, and the clustering probability in bulk can be easily calculated following this new correlation, in particular for further calculation which imply higher PKA energies.

5.4 Binary collision approximation

In this part of the thesis, we concentrated in comparing analytical models proposed by Norgett-Robinson-Torrens and Kinchin-Pease to MD results to calculate the total displacements after cascades.

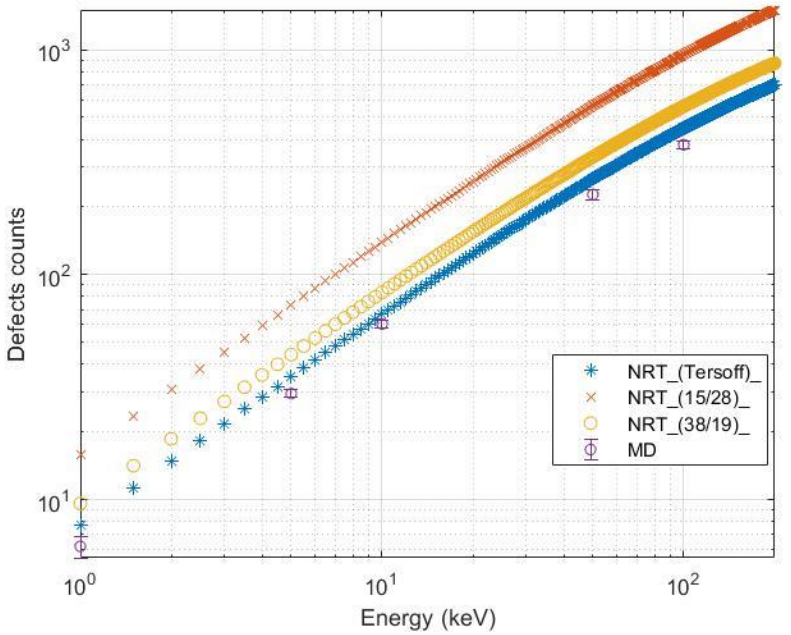

Figure 5.5.1: Comparison of NRT formulas with different values of TDE (TDE_{Si}=46 eV TDE_C=36 eV calculated with Erhart-Albe potential in blue, TDE_{Si}=15 eV TDE_C=28 eV using the values suggested in TRIM in red, TDE_{Si}= 38 eV TDE_C=19 Ev suggested on DFT calculations in yellow)

To build the NRT curves in the graph above we used different values of threshold energies: in blue we represented the displacements calculated with EA05 potential in MD simulations, in yellow the displacements calculated with the averaged TDE proposed by DFT calculation proposed in the article of Lucas et al. and in red the TDE proposed by default in TRIM.

In the picture, only Si and C vacancy have been represented for both NRT and MD values. It is of interest to note that the total number of defects produced in SiC is generally lower than that predicted by the NRT formula.

The NRT equation used for this study was originally applied to metals and its application to multicomponent compounds is not straightforward because each element in the compound (Si and C) has different threshold energies and antisite defects can be produced. In applying the above equation, the antisite defects have not been included in the picture.

From the figure we observer reasonable agreement between the MD and the NRT results calculated with the threshold energy estimated using molecular dynamics. While the NRT which used the same TDE as MD simulation has a margin of 18% with the MD results, the NRT with E_d derived from DFT shows a margin of almost 50%.

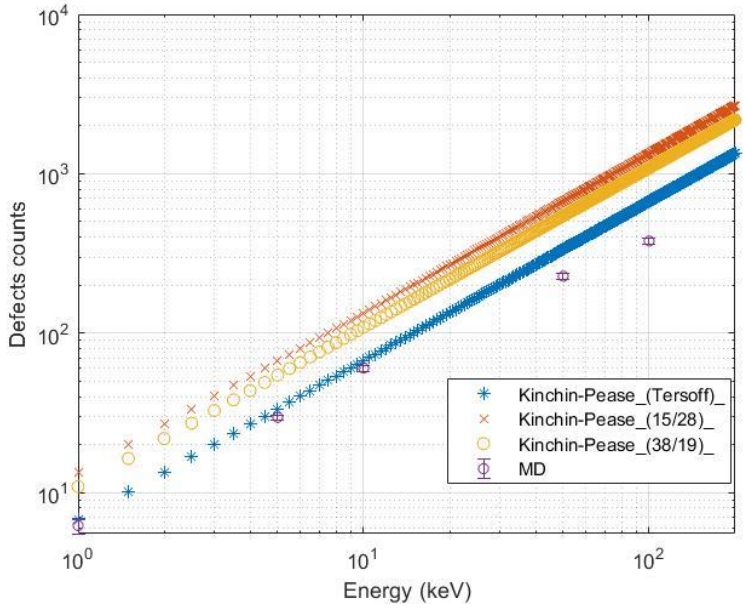

Figure 5.5.2: Comparison of SiC defects calculated with values of TDE for the Kirchin-Pease formula (1974) (TDE_{Si}=46 eV TDE_C=36 eV calculated with Erhart-Albe potential in blue, TDE_{Si}=15 eV TDE_C=28 eV using the values suggested in TRIM in red TDE_{Si}= 38 eV TDE_C=19 Ev suggested on DEFT calculations in yellow)

The modified Kinchin–Pease model provides a reasonable estimate of defect production in SiC only at low damage energies, but overestimates the defect production at energies of several keV and higher with respect to the NRT formula.

In the following graph we calculated the defect production efficiency of NRT and Kirchin-Pease (KP) models as follows:

$$\varepsilon = \frac{\text{defects}_{\text{NRT,KP}}}{\text{defects}_{\text{MD}}} \tag{5.3}$$

while the error has been calculated as

$$error = C\frac{dx}{x^2} \tag{5.4}$$

Where C represents the number of defect calculated using the analytical models, dx the error of the MD results and x the MD results.

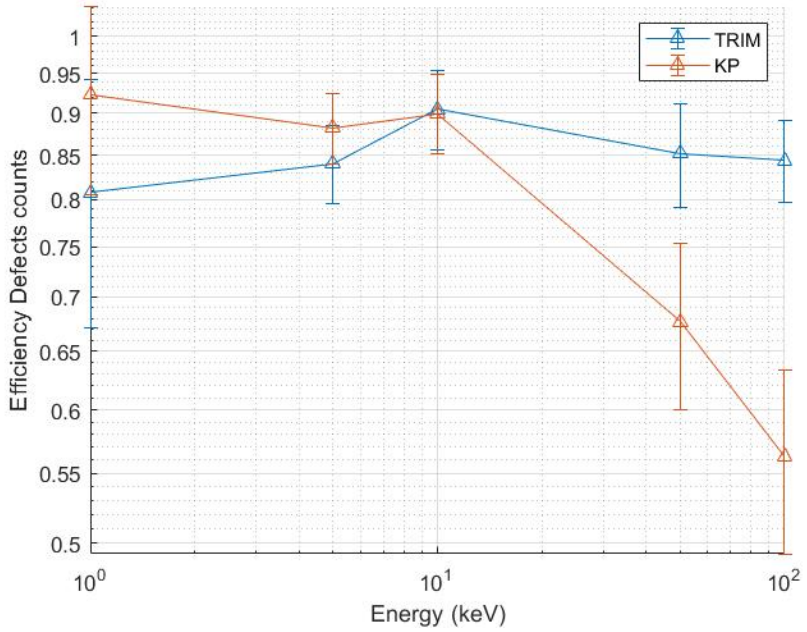

Figure 5.5.3: Defect production efficiency as a function of PKA damage energy.

Although the defect production efficiency in SiC decreases almost continuously with increasing PKA energy, similar to behavior in metals, the relative damage efficiency is much higher in SiC compared to metals [49]. Only for 10keV it is possible to see an increase in the efficiency for both NRT and KP method, which can be justified as a lack of statistics (only 10 independent simulations for MD). In this study it is possible to see that the use of E_d respectively equal to 36 eV for C and 46 eV for Si which were used to calculate N_{disp} , gives a resulting defect production efficiency exceeded 0.8 for almost all PKA energies.

In this part of the study, computer simulations based on the binary collision approximation (BCA) and molecular dynamics (MD) methods are employed to determine the dependence of displaced atom production on the damage energy of the primary knock-on atom (PKA). The damage energy is the kinetic energy of the PKA that is dissipated by nuclear collision processes (nuclear stopping), with the remainder of the PKA energy being dissipated by ionization and electronic excitation processes (electronic stopping) (see previous part). What we expect, combining the friction force calculated in TRIM with MD is that the BCA

simulations should appear in good agreement with MD results. This is because not a lot of clustering is going on in SiC. In fact, the number of subcascade is limited and in bulk large clusters were not present. BCA methods are not many-body type (as seen for MD using Tersoff potential), and in binary collision, clusters are not counted. This is the motivation why the results obtained in TRIM calculations are expected to be in good agreement with MD ones.

By comparing the results of MD and BCA simulations over a range of energies, the understanding of damage productions on the Si and C sublattices in SiC will be improved, which will lead to faster procedures for the defects production in SiC.

The number of displaced Si and C atoms as a function of PKA damage energy have been determined using the new version of SRIM code (2008).

Based on the statistics for a limited number of MD simulations (10 non overlapping simulations for each PKA energy), the average numbers of vacancies produced on the Si and C sublattices in 3C–SiC have been determined in SRIM as function of PKA energy, as shown in the picture below.

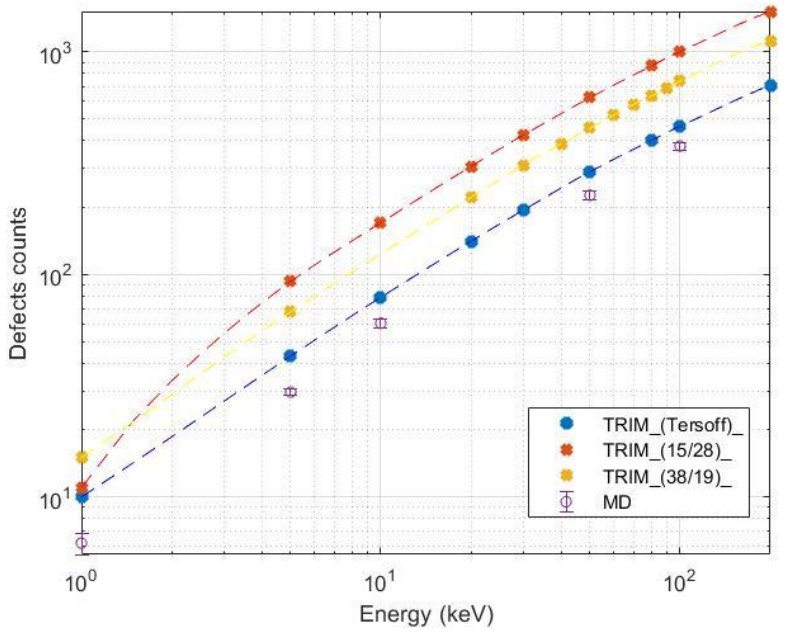

Figure 5.5.4: Comparison of TRIM computational results calculated with different values of TDE (TDE_{Si}=46 eV TDE_C=36 eV calculated with Erhart-Albe potential in blue dots, TDE_{Si}=15 eV TDE_C=28 eV using the values suggested in TRIM in red dots TDE_{Si}= 38 eV TDE_C=19 Ev suggested on DEFT calculations in yellow dots)

At all energies, the number of defects produced by Si PKAs in SRIM and the number of defects produced by Si PKAs in the MD simulations are, within statistical uncertainties, in reasonable agreement with the SRIM results with a detachment of more than 30%, which suggests that the threshold displacement energies used in the SRIM simulations are not unreasonable even though slightly higher values, probably, would provide better agreement.

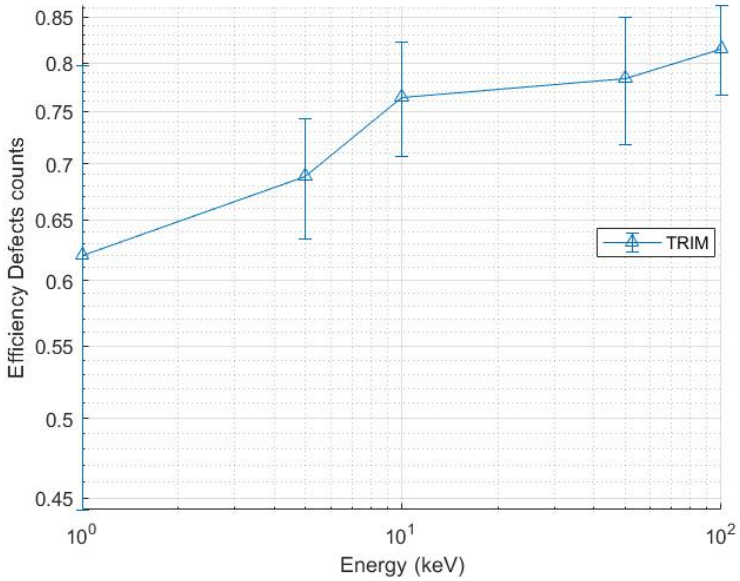

Figure 5.5.5: Defect production efficiency as a function of PKA damage energy in TRIM.

The total damage efficiency for Si PKAs is shown in the figure above. The increase in damage efficiency with increasing damage energy up to ε=0.8. Nevertheless, the tendency described by the figure above can be attributed to the presence of more ballistic effects when the energy gets higher and higher. In fact the ratio between pockets formation is not directly proportional to the energy ratio, but noticeably inferior.

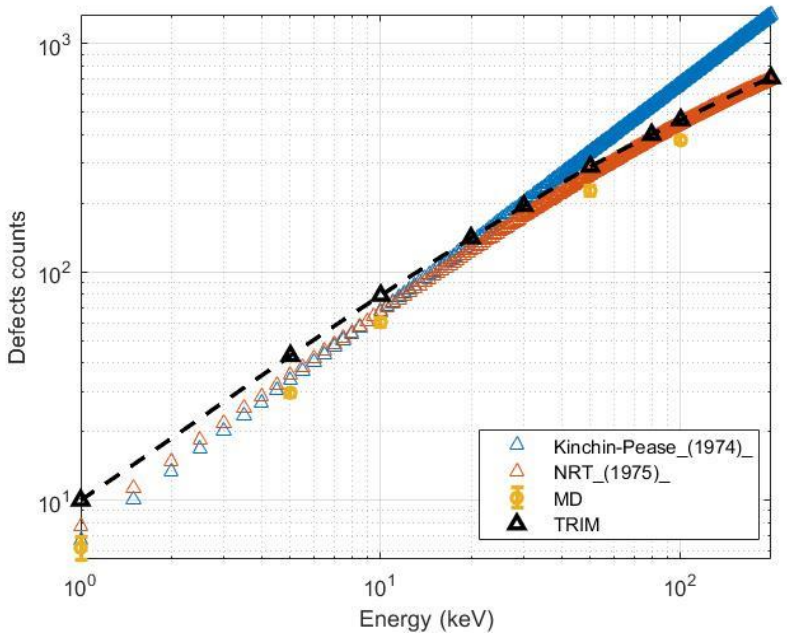

Figure 5.5.6: Evaluation of SiC defects calculated using the Kirchin-Pease formula, using the closest approach approximation. Comparison of TRIM computational results, Kirchin-Pease, NRT (1975) formula with molecular dynamics results TDE values from Erhart-Albe potential (TDE_{Si}=46 eV TDE_{C}=36)

To conclude this part, as shown in the figure above, MD and SRIM computational results get closer and closer for higher energies, differently from Kirchin-Pease and NRT models. From the previous analysis, TRIM and BCA analytical formula results are close to the ones defined in MD simulations.

This conclusion justifies the use of BCA to simulate the total amount of defects. In fact, based on the size distribution of clusters, we can determine their total amount in the material bulk and possibly extrapolate it to higher PKA energy.

As a result of these conclusions, we decided that the application of a long-time simulation method would extend the reach of the results presented here and provide a more complete answer to the question from the introduction, *`How does the initial distribution of defects evolve in time?*', as such as mesoscale methods like KMC (Kinetic Montecarlo Methods).

This idea allows for long time simulations of infrequent events as one needs not to select the timestep manually or proceed with a small (i.e. femtosecond scale) timestep throughout the course of the simulation in order to capture every transition event.

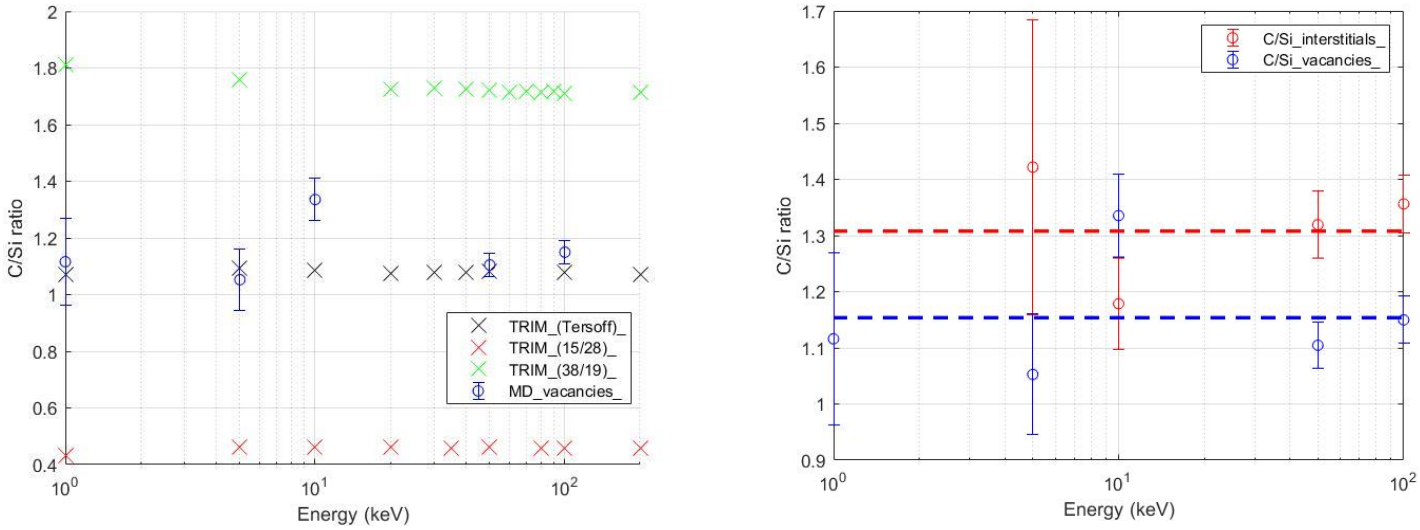

Figure 5.5.7: A) The results in the graph represent the C/Si ratio for vacancies using TRIM compared with those reported for MD calculations. It is possible to see that C/Si ratio calculated for MD results is in good agreement with that calculated for TRIM in which it was used the TDE values calculated with Erhart-Albe potential.
B) C/Si ratio for interstitials defects and vacancies defects reported for SiC. It is possible to see a constant tendency for both C/Si ratio defined for vacancies and interstitials.

The ratios of C vacancies/interstitials to Si vacancies/interstitials are shown in the figure (A) above for all the MD simulations and the SRIM simulations and empirical formula (NRT and KP) for Si PKAs.
Based on SRIM simulations, the ratio of C/Si vacancies should saturate at about 1.1 above 1 keV.
The blue circles in the figure are the C/Si ratios determined from the MD data. The trend suggests that there may be some convergence of the C/Si ratios at higher damage energies with SRIM results as it was possible to see from the damage efficiency, but demonstrating

this in MD simulations would have required a larger number of simulations which were not require for the present work. It is interesting to notice that for TDE which corresponds to DFT data the C/Si ratio is higher (1.8 vs 1.1/1.3 found for MD) due to the very low value of C threshold energy (19 eV compared to 36eV found for Erhart-Albe/ZBL potential) which is due to the enhancing of C displacements in respect to MD simulation. On the opposite side, we find the C/Si ratio for SRIM simulation for the TDE suggested from SRIM. In this case, it is Si sublattice to have the lower E_d value, which justify the low value of the ratio.

In the figure (B) it is possible to see C/Si ratio calculated with the results obtained only in MD for both vacancies and interstitials.

We can notice that C/Si ratio for 1 keV has not been reported. In the analysis we found that no Si atoms were present in the interstitials formed after the cascade. In fact, Si/C→0 at 1 keV PKA. This value can be seen as the result of lack of statistics (only 10 runs have been performed for each PKA energy value) or during recombination, Si interstitial defects tends to recombine faster than C defects.

Therefore, the average ratio calculated for vacancies is 1.15 while for interstitials 1.30.

The average values have been calculated in the following way:

$$R_{ave} = \frac{1}{\sum_i \frac{1}{error_{std,i}}} \cdot \sum_i \frac{1}{error_{std,i}} R_i \qquad (5.5)$$

Where R_{ave} corresponds to the average C/Si ratio for both vacancies and interstitials, $error_{std,i}$ is the standard error calculated for each result and R_i is the C/Si ratio calculated for each PKA energy.

The difference observed between $R_{ave,interstitials}$ and $R_{ave,vacancies}$ is due to the fact that the formation energy of interstitial carbon is much lower than Si, so more C in interstitials are found in cluster.

5.6 Interfaces SiC/graphite

5.6.1 Interface energy

Interfaces often play a determining role in the properties of polycrystalline solids. Much recent research on novel structural materials aims to exploit the influence of interfaces [50], e.g to heal radiation damage, improving their tensile strength, thermal conductivity, and other properties [51][52]

For the SiC/graphene, the previous researches mainly focus on the interfacial thermal conductance, electronic structure, and some other properties mainly for electronic devices, since SiC is an efficient semiconductor [53][54].

Recently research concentrated on the interatomic interaction between graphite and SiC using MD simulation for its effect on interfacial thermal conductance [50]. Moreover, another MD simulation work about the SiC/graphite revealed that the first a few SiC atomic layers closest to the interface are easily damaged in ion irradiation simulations [50].

Little is known about how the SiC/graphite interface alters defect migration and clustering. The SiC/graphite interface is reported to be similar to a grain boundary. Though molecular dynamics has never been used to study an SiC/graphite interface but it has been used to observe radiation damage on SiC grain boundaries. Swaminathan et al. conducted ion irradiation simulations on bicrystal SiC and found that the damage in the in-grain region was unaffected by the presence of a grain boundary [55].

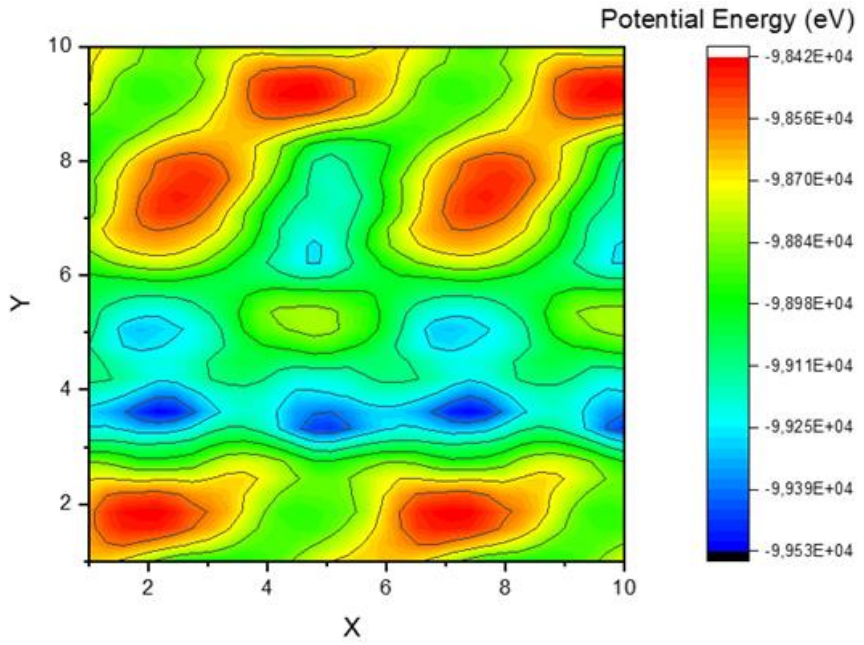

Figure 5.6.1: Color map representing the [001] SiC/graphite interface system potential energy. The scope of the image is furnishing a visual representation of those configuration which have lower potential energy and so which are more stable. In red the most stable configuration. For our calculation we chose those interface which coordinates are x=23 and y=10.

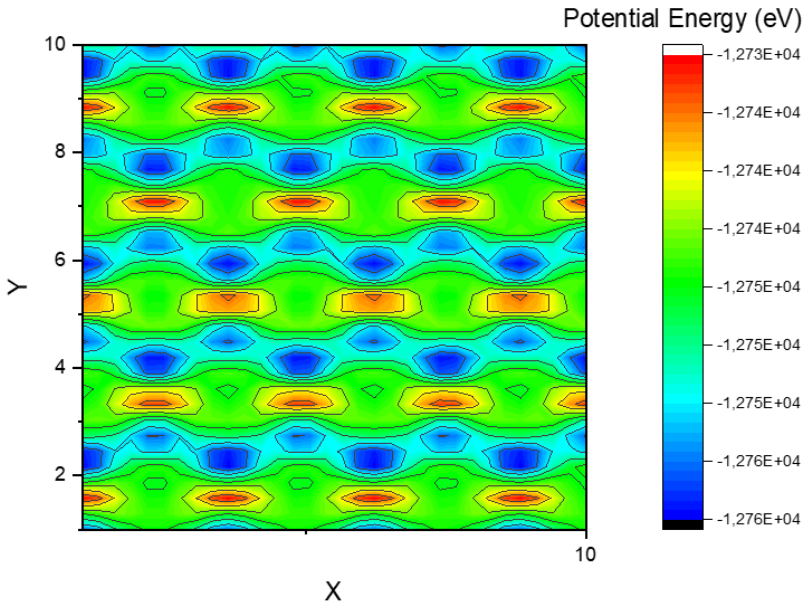

Figure 5.6.2: Color map representing the [111] SiC/graphite interface system potential energy. The scope of the image is furnishing a visual representation of those configuration which have

lower potential energy and so which are more stable. In red the most stable configuration. For our calculation we chose those interface which coordinates are x=50 and y=37.

In the figures above we represented a color map related to the total potential energy of a system formed by SiC and graphite. The scope of this part of the project is to see what interface owns the lower potential energy, which also consists in finding the most stable configuration.

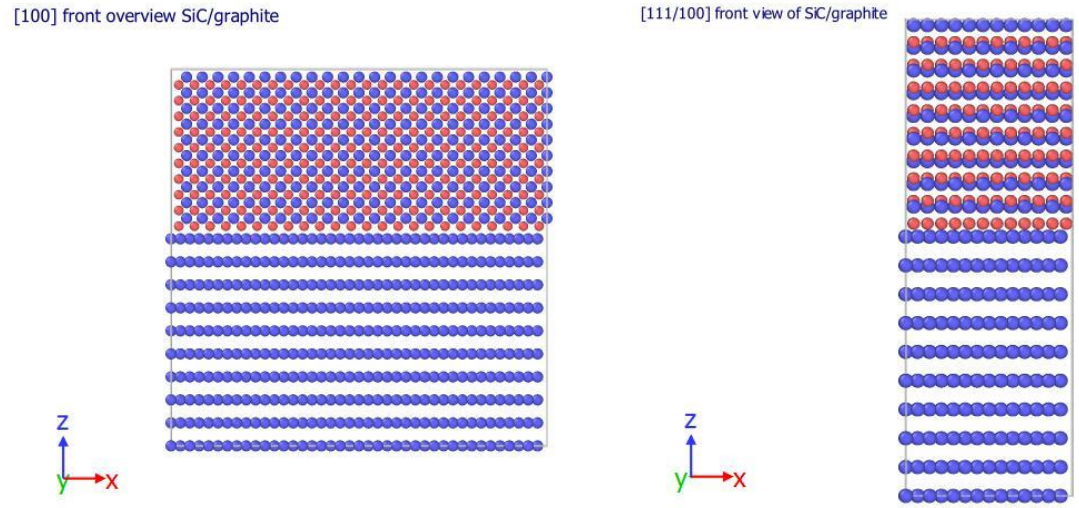

Figure 5.6.3: [001/001] SiC/graphite interface front overview and [111/001] SiC/graphite interface front view most stable configuration.

The first step consists in the definition of the configuration of the two types of interfaces. In the first figure, both SiC and graphite are on [001] direction, while in the second picture only SiC is oriented along the [111] direction.

After building the two configuration we translated the atoms of the SiC over the x and y direction with a step of 1/50 of the size of the box. After, in LAMMPS, we calculated the potential energy of the system for each translation. During the atoms translation some of the coordinates exceeded the box size, s, since the box has finite size, periodic boundary conditions were maintained.

The results have been collected and represented in heat color maps in which red represents the lowest value of the potential energy, while blue the highest value, characterized by periodicity.

Directions	# step x	# step y	Potential energy [eV] (before minimization)	Potential energy [eV] (after minimization)
[100/100]	23	10	-99525.312	-105142.01
[111/100]	50	37	-12759.2	-15443.892

Table 5.6.1: Potential energy of the most stable configurations of [100/100] and [111/100] SiC/graphite interface

The following stage consisted in minimizing the potential energy of the systems we chose based on the previous analysis keeping constant the volume of the boxes listed in Table 5.6.1.

Interface Energy calculation						
	SiC	Graphite	interface_area	total_energy	**Interface Energy (eV/A^2)**	**J/m^2**
[100/100]	-36513.6	-70790.4	2736.1269	-105142.010	0.395	**6,329**
[111/100]	-5477	-10323.6	394.9259	-15443.892	0.4517	**7,236**

Table 5.6.2: Interface Energy calculation of the most stable configurations of [100/100] and [111/100] SiC/graphite interface

In Table 5.6.2 we presented the total interface energy for [001/001] and [111/001] SiC/graphite interface in J/m^2. As it is possible to see, the [001/001] SiC/graphite shows the lowest energy, which is an unexpected results. As reported in literature from previous experimental works [56][57][58] in the case of the Si face of SiC (001), the graphitization process is slow, and it is easy to control the number of graphene layers, while for a C-terminated surface the graphitization process is very fast and a large number of graphene

layers are formed. Nevertheless, the most suitable surface remains 3C SiC (111). Because of this, we expected to find interface energy lower for SiC(111) oriented.

This results can be explained because of the periodicity of the boundary conditions that gives as a result only an average value of the energy of the interface, since the atom layer of SiC in contact with the graphite changes depending on the position of the interface.

Because of this, it has been proposed to use the semi-infinite crystal method. However, this is a complex non-standard method that is outside the scope of the present thesis.

5.6.2 Binding Energy of point defects to interfaces

In this part of the thesis we are interested in finding the binding energy between the defects created in proximity of the interface in function of the distance.

To assess trapping of point defects at SiC-graphite interfaces, the binding energy energies of vacancies and interstitials at these interfaces were computed in function of the distance from the first carbon layer of the graphite. On the interface structure C and Si layers were alternated and free surface has been created over SiC and graphite boxes; after, vacancies were created by deleting an atom, and interstitials by inserting an atom at a desired location. Defect structures were relaxed at constant volume through conjugate gradient energy minimization to relax configurations with closely spaced atoms that may arise due to interstitial/vacancy insertion.

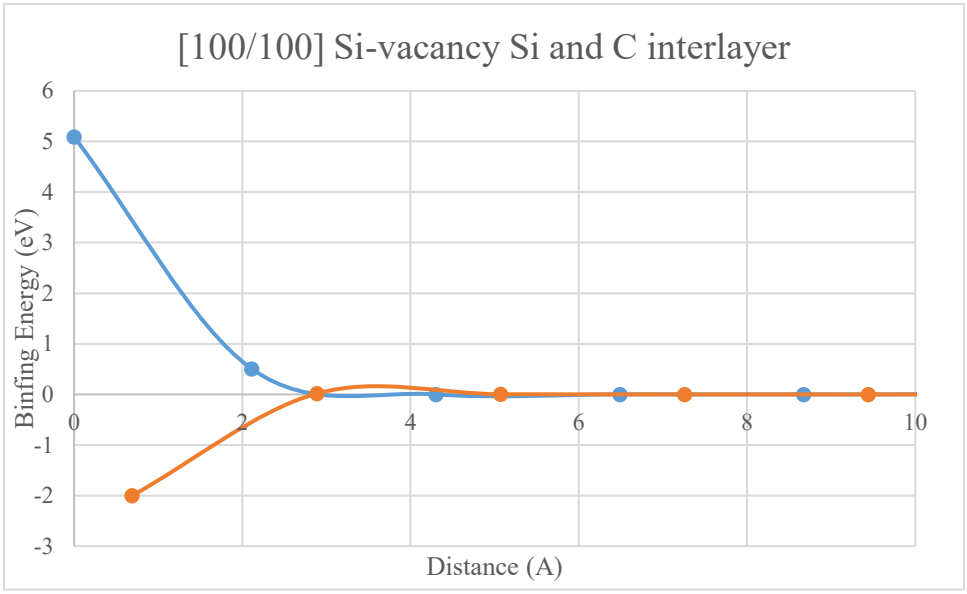

Figure 5.6.4: The figure represents the binding energy between Si vacancy created in the system alternating first Si layer (in blue) and C layer (in red) on the interface.

In the figure above we computed the binding energy of the Si-vacancy as a function of the distance from the interface. The first point for both the curves indicates the nearest inserted Si-vacancy to the interface. The binding energies are indicative for the binding energy of an impurity to a particular site with positive values indicating bonding. In fact, it is possible to see that the binding energy is positive for Si-vacancy in case of Si layer over the graphite, inducing the interface to work as a sink for point defects. This energy diminishes until reaching zero in the bulk, where the vacancy doesn't feel any type of interaction. On the opposite sense, Si vacancy have negative binding energy when a C layer is set on the interface, showing that, in this case, the interface doesn't behave as a sink.

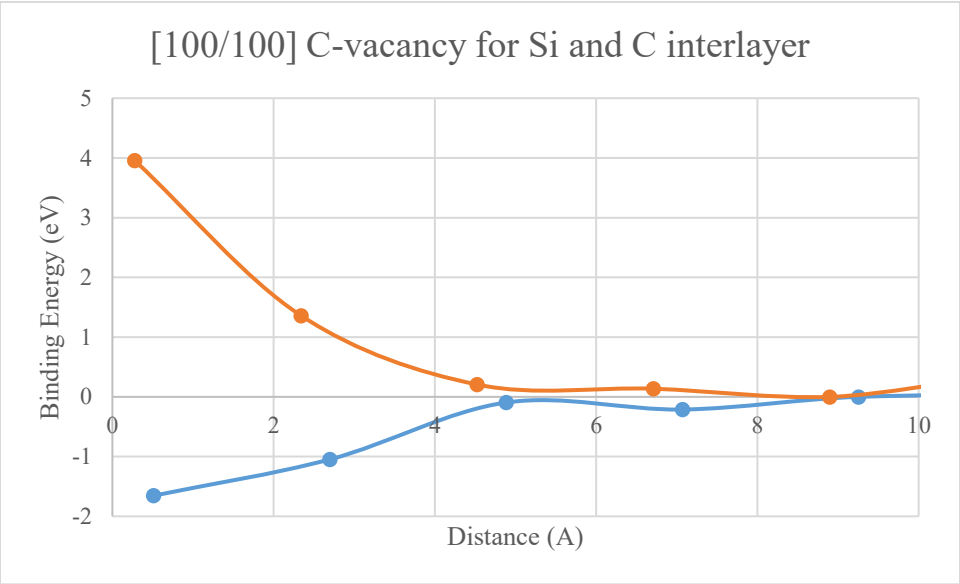

Figure 5.6.5: The figure represents the binding energy between C vacancy created in the system alternating first Si layer (in blue) and C layer (in red) on the interface.

In this case, the trend of the curve is exactly the opposite than the first picture. A C vacancy is repelled from the interface when a Si layer is set over. On the other hand, the defects are attracted to the interface when a C layer is set over the interface.

For [111/100] SiC/graphite interface, the computation of the binding energy is more complicated since more structures of interface can be considered.

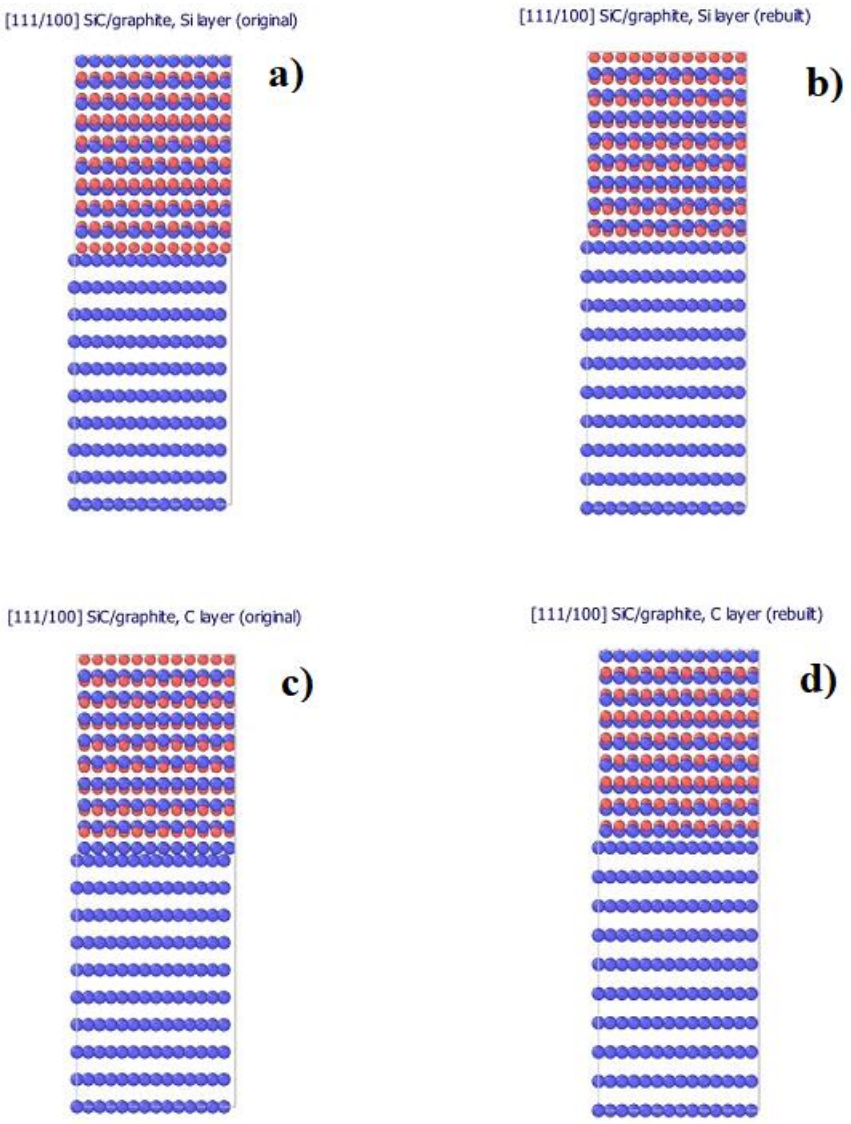

Figure 5.6.6: Non relaxed [111/100] SiC/graphite interface: a) original structure with Si layer, b) rebuilt structure with Si layer, c) original structure with C layer, d) rebuilt structure with C layer

First, we alternated the carbon and the silicon layer over the interface as we did previously for the [001/001] SiC/graphite interface. The results are reported in the graphs below.

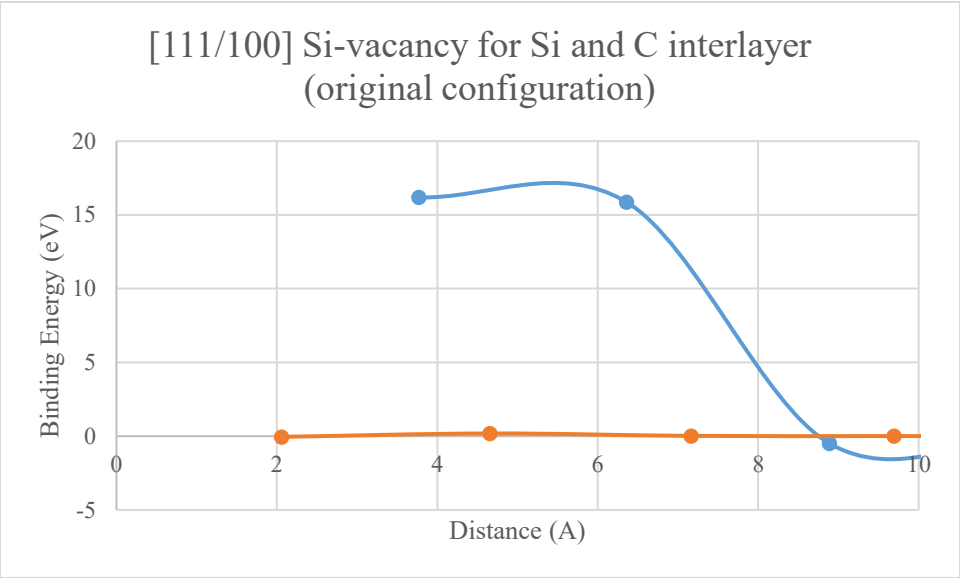

Figure 5.6.7:The figure represents the binding energy between Si vacancy created in the original system alternating first Si layer (in blue) and C layer (in red) on the interface.

Similarly to the first picture representing a Si and C layer on [001/001] SiC/graphite interface also in this case a Si vacancy has a positive binding energy when there is a Si layer at the interface, which decreases when the distance from the interface increases. However, for this structure, the binding energy of the vacancy to the interface is almost 3 times bigger than the [001/001] SiC/graphite interface. Almost constant to zero is, on the other hand, the binding energy of a Si vacancy when there is a C layer on the interface, but on the interface it tends to become slightly repulsive.

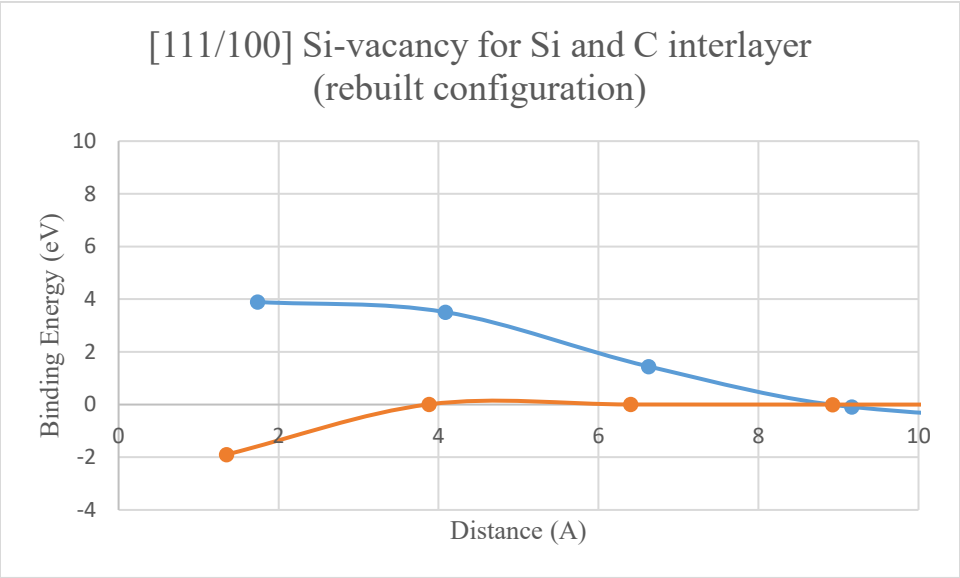

Figure 5.6.8: The figure represents the binding energy between Si vacancy created in the manually rebuilt system alternating first Si layer (in blue) and C layer (in red) on the interface.

Similarly to the previous picture representing a Si and C layer on [111/001] SiC/graphite original interface also in this case Si vacancy have positive binding energy in the case of a Si layer over the interface which decreases in function of the distance from the interface. However, for this structure, the binding energy of Si vacancy near the interface is similar to the [001/001] SiC/graphite interface. On the other hand, the binding energy of a Si vacancy when there is a C layer on the interface is negative and repulsive as expected.

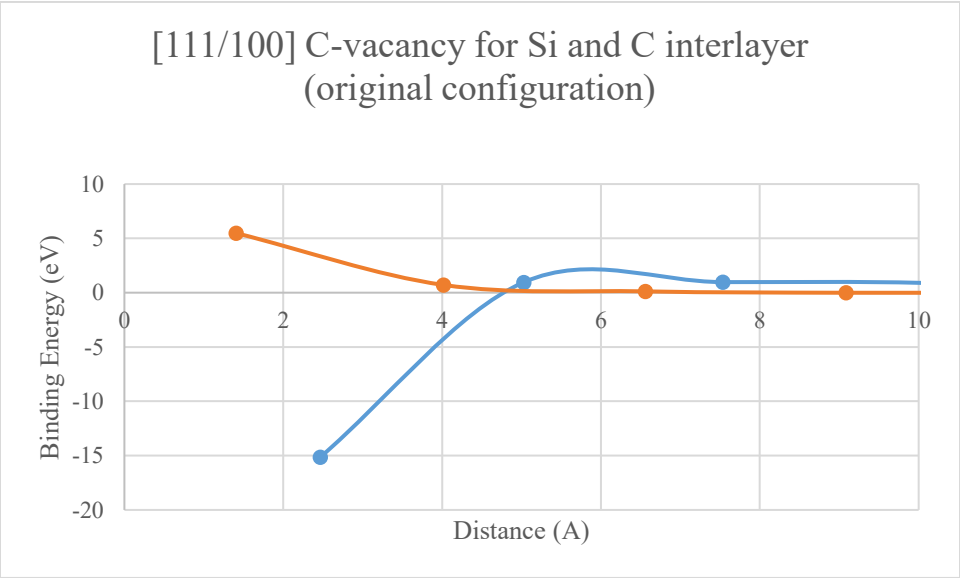

Figure 5.6.9: The figure represents the binding energy between C vacancy created in the original system alternating first Si layer (in blue) and C layer (in red) on the interface.

As previously seen for [001/001] SiC/C interface the trend of the curve is exactly the opposite than the first cases as we expected. A C vacancy is strongly repelled from the interface when a Si layer is in contact with the interface (almost 7 times more negative than for the [001/001] SiC/graphite interface). On the other hand, the defects is attracted to the interface when a C layer is set over the interface, showing similar values as for [001/001] interface.

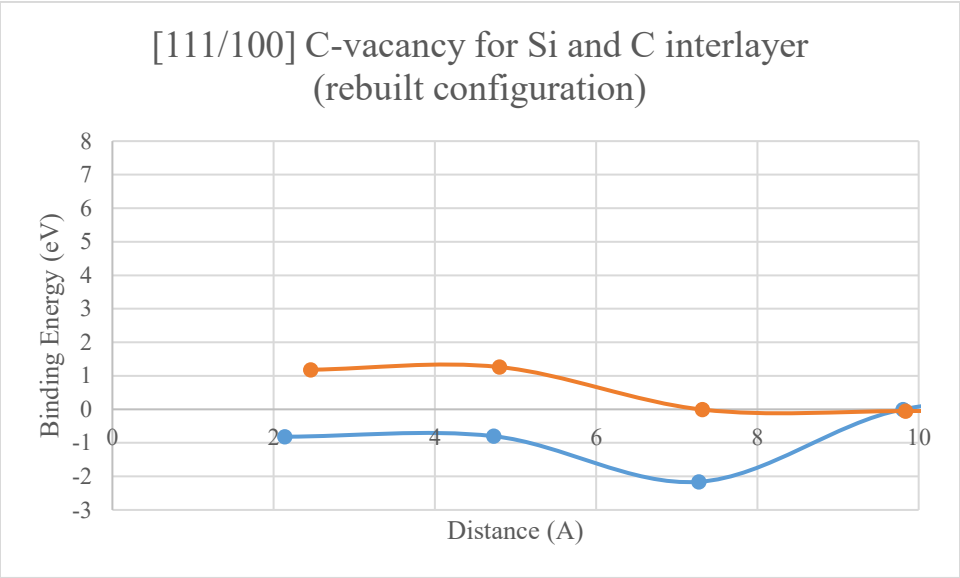

Figure 5.6.10: The figure represents the binding energy between C vacancy created in the manually rebuilt system alternating first Si layer (in blue) and C layer (in red) on the interface.

Similarly to the previous figure representing a Si and C layer on a [111/001] SiC/graphite interface, also in this case a C vacancy has a positive binding energy in the case of C layer over the interface, which decreases as a function of the distance from the interface. However, for this structure, the binding energy of a C vacancy near the interface is weakly positive in contrast to the case of a Si layer. Nevertheless, in case of a Si layer, we can see an oscillatory behavior between 5 and 10 A of distance where the binding energy alternates values between 0 and -2 eV. This can be explained by poor convergence of the relaxation process of the structure.

In the last two figures, we focused on the [001/001] SiC/graphite interface, which resulted in having the lowest averaged interface energy to calculate the binding energy between the interstitials and the interface in function of distance.
Differently from the previous analysis for vacancies, the interstitials binding energy resulted to be less smooth.

The lowest defect formation energy has been attributed to the $C_{<100>}$ dumbbell interstitials with 5.07eV. The interstitial defect was inserted manually in the SiC lattice and the system was relaxed.

We obtained the following results.

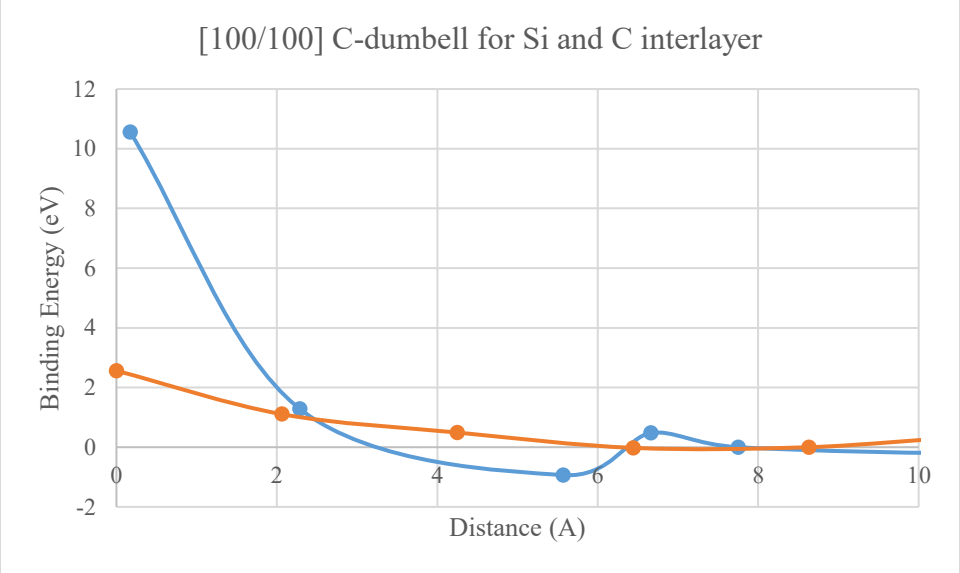

Figure 5.6.11: The figure represents the binding energy between $C_{<100>}$ dumbbell created in the system alternating first Si layer (in blue) and C layer (in red) on the interface.

Differently from vacancy inserted in the same system, this time, for both C and Si layer, the binding energy of the C(I) at the shortest distance from interface is positive. It is largely attractive for a Si layer, with a difference of 8eV between the two types of interface.

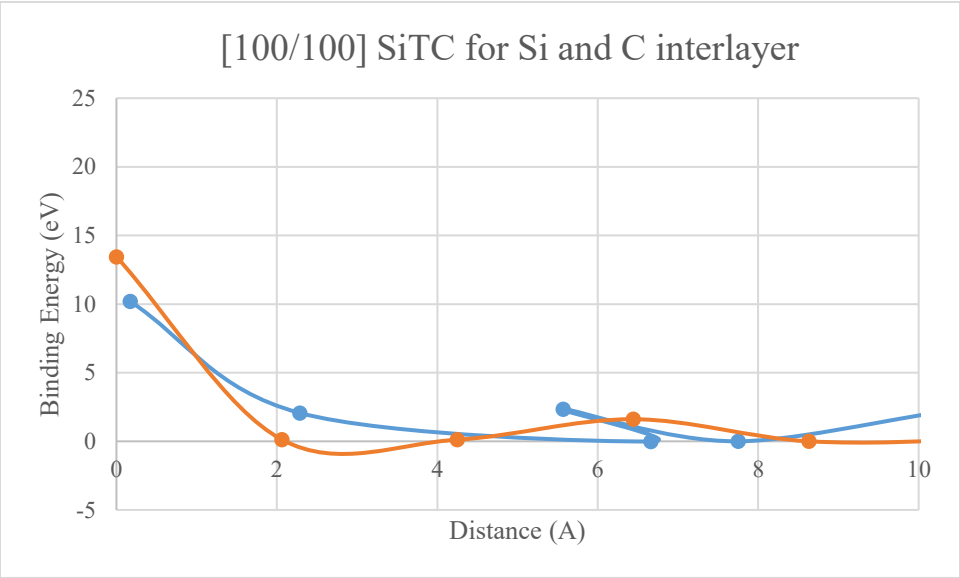

Figure 5.6.12: The figure represents the binding energy between tetrahedral *interstitial* Si_{TC} *created in the system alternating first Si layer (in blue) and C layer (in red) on the interface.*

Also for this configuration we see that for both C and Si layer, the binding energy of the C(I) at the shortest distance from the interface is positive with almost the same value.

Chapter 6

6. Summary and Conclusions

In recent years, computational models have claimed an important role in understanding the mechanisms at work leading to the degradation of materials under irradiation. The phenomenon of radiation in materials is inherently a multi-scale problem: a flux of subatomic particles (neutrons) interacts with lattice atoms leading to the failure of macroscopic components. Given the different length- and time scales involved, multi-scale modelling techniques are used to simulate the damage mechanisms active at the different scales of the radiation process.

In this thesis we aim to contribute by providing input data to meso-scale models by means of atomistic simulations.

Chapter 1 of this dissertation provided a review of the literature regarding the utilization of 3C-SiC and SiC fibers (e.g SiC/SiC, SiC/PyC, Tyranno…) nuclear power applications and industry.

For atomistic simulations, a PKA kinetic energy between 1 and 100 keV were chosen for its relevance to both fusion and fission applications as well as being within the energy range where classical molecular dynamics simulations of atomic collisions are valid.

In Chapter 2 there is a brief description of the workplan of the thesis.

Chapter 3 is dedicated to the results obtained using different empirical potentials in molecular statics to find the formation energy of each point defects for both SiC and graphite. The most stable configurations is found in literature to be $CC_{<100>}$ dumbbell interstitial for carbon, while Si_{TC} is the most stable configuration reported in literature for

Si in 3C-SiC. For graphite, on the other hand, the spiro structure wss found to be the most stable defect from DFT results. In conclusion, we found that only Erhart-Albe empirical potential was in accordance with the predicted results obtained in DFT.
Moreover, Chapter 3 focuses on how the nuclear and electronic stopping power contributes in molecular dynamics to receive more accurate results; through the use of SRIM in this section, we found a linear fitting curve which combine the velocity with the predicted kinetic energy of the incoming particle.

The last part of Chapter 3 is also dedicated to calculate the TDE necessary to implement the cascade on TRIM and finding the correct results while using the empirical formulas. In general, the TDEs calculated with the potential used here have been compared with experimental and DFT results obtained from other authors. The TDE variations found in this work were attributed to subtle differences in the definition of different stiffening. It was concluded that the potential performed sufficiently well to justify its use.
The final section of the third chapter is completely dedicated to empirical formulas proposed in literature to generate the total number of displacements in studied materials. This results have been compared with those found using TRIM simulations and MD dynamics, seeing that, for TRIM there is an increase on Defect production efficiency as a function of PKA damage due to the fact that in there is the presence of more ballistic effects when the energy gets higher and higher and, since TRIM cannot predict clustering and/or recombination effects, it means that defects don't have a very high probability to form large clusters at high PKA-energy. We could conclude from this study that TRIM and similar BCA programs can be a substitute to MD for the generation of point defects in SiC.

Chapter 4 is dedicated to the description of the atomic structure of both SiC and graphite. We dedicated the final part of Chapter 4 to the characteristics of the point defects which can form after the radiation damage in the bulk of the two compunds.

Chapter 5 is related to the verification procedure. It consists in the reproduction of the 1 to 100 keV Si PKA cascade simulations in a perfect silicon carbide crystal with no thermal effects on the damage state. The results showed good qualitative agreement with the published results, verifying the simulation and post-processing procedure. This part is the key part of our work, since it has been possible, through the defect analysis performed in Ovito, to extract the statistical clustering (vacancy and interstitial) distribution in SiC bulk for given PKA energy, which is completely new in terms of available literature on the argument.

The main outcome of these results is that, using the mathematical formula derived from the distribution, it will be possible to find the total number of clusters in SiC bulk without the auxiliary of MD simulations, extremely time consuming compared to BCA methods.

This information will be used to generate the clusters distribution studied in the long-time calculations in future works. Probably, further simulations and statistical analysis is required to improve the quality of the spatial distributions, though those calculated here provided a good initial approximation.

We found that the C/Si ratio necessary as an input for KMC programs to detect the evolution of the defects for larger arc of time.

We found for vacancies C/Si ratios that TRIM and MD gives approximately same results and the fact that for interstitials C/Si is ratio is higher in value in respect to vacancies is due to the fact that formation energy of interstitial carbon is much lower than Si, so more C in interstitials are found in cluster.

The final part is dedicated to SiC/graphite interface. Interfaces play a big role in industrial sector, in particular when subjected to irradiation. Not many studies have been performed of SiC/graphite interface, but in the last years these are intensifying also because of its use in TRISO technologies.

Interface energy calculations have been performed for two differently oriented SiC/graphite interfaces: in the first one SiC is [100] oriented while in the second case SiC is [111] oriented. It has been found, in contradiction with literature, that SiC[100]/graphite interface

has a lower interfacial energy of SiC[111]/graphite interface. This has been explained as the total interface energy in our work correspond to an averaging of the energies found for C and Si layers that can be alternated on the surface. Moreover, it has been found essential performing the same calculation for semi-infinite crystal which was not possible to compute in LAMMPS.

Defects (vacancies and most stable interstitials) have been injected in the system and we calculated the total binding energy between the defect and the interface in function of the distance, alternating C and Si layers over the interface and eliminating the results which corresponds to free surface.

It has been found that the binding energy is included between -5 eV (repulsive binding energy, the defect is not absorbed in the sink) and +15 eV (attractive binding energy, the defect tends to migrate on the sink), values which have been expected from the available literature.

In conclusion, the main contributions of this work are:

- Quantitative characterization of the statistical distribution of vacancy and interstitial clusters after simulated cascade formation in 3C-SiC.
- Utilization BCA methods for detection of 3C-SiC damage simulated in cascade formation in bulk
- Input for KMC calculations: C/Si ratios found for both interstitials and vacancies
- Initial study of SiC/graphite interface from the molecular statics point of view

Based on the experience gained during this work the following are recommended as avenues of future research that directly build on the work in this dissertation:

On SiC and graphite materials:

- Stability of point defects and point defect clusters over timescales much greater than 10 ps.
- Damage cascade simulation in graphite bulk performance.

On SiC/graphite interfaces:

- Multiple and different position and direction should be taken into consideration.
- The use of semi-infinite crystal boundary condition.
- Cascade simulations using MD on interfaces should be performed using the same potential.

Bibliography

[1] G. R. Fisher and P. Barnes, “Towards a unified view of polytypism in silicon carbide,” *Philos. Mag. B*, vol. 61, no. 2, pp. 217–236, Feb. 1990.

[2] T. Hojo *et al.*, “Radiation effects on yttria-stabilized zirconia irradiated with He or Xe ions at high temperature,” *Nucl. Instruments Methods Phys. Res. Sect. B Beam Interact. with Mater. Atoms*, vol. 241, no. 1–4, pp. 536–542, Dec. 2005.

[3] G. A. Slack and R. I. Scace, “Nitrogen Incorporation in SiC,” *J. Chem. Phys.*, vol. 42, no. 2, pp. 805–806, Jan. 1965.

[4] B. Collin, “Comparison of fission product release predictions using PARFUME with results from the AGR-1 safety tests,” Idaho Falls, ID (United States), Sep. 2014.

[5] S. B. Grover, D. A. Petti, and J. T. Maki, “Completion of the First NGNP Advanced Gas Reactor Fuel Irradiation Experiment, AGR-1, in the Advanced Test Reactor HTR 2010 Completion of the First NGNP Advanced Gas Reactor Fuel Irradiation Experiment, AGR-1, in the Advanced Test Reactor,” 2010.

[6] Y. Katoh, K. Ozawa, T. Hinoki, Y. Choi, L. L. Snead, and A. Hasegawa, “Mechanical properties of advanced SiC fiber composites irradiated at very high temperatures,” *J. Nucl. Mater.*, vol. 417, no. 1–3, pp. 416–420, Oct. 2011.

[7] L. L. Snead, T. Nozawa, Y. Katoh, T.-S. Byun, S. Kondo, and D. A. Petti, “Handbook of SiC properties for fuel performance modeling,” *J. Nucl. Mater.*, vol. 371, no. 1–3, pp. 329–377, Sep. 2007.

[8] W. Katoh, Snead, Burchell, “Composite Materials for High Temperature Reactors: Technology Development Roadmap,” in *Conference: 5th International Conference on High Temperature Reactor Technology*, 2010.

[9] Y. Katoh, L. L. Snead, I. Szlufarska, and W. J. Weber, “Radiation effects in SiC for nuclear structural applications,” *Curr. Opin. Solid State Mater. Sci.*, vol. 16, pp. 143–152, 2012.

[10] Y. Katoh, N. Hashimoto, S. Kondo, L. L. Snead, and A. Kohyama, “Microstructural development in cubic silicon carbide during irradiation at elevated temperatures,” *J. Nucl. Mater.*, vol. 351, no. 1–3, pp. 228–240, Jun. 2006.

[11] Y.-R. Lin, C.-S. Ku, C.-Y. Ho, W.-T. Chuang, S. Kondo, and J.-J. Kai, “Irradiation-induced microstructural evolution and swelling of 3C-SiC,” *J. Nucl. Mater.*, vol. 459, pp. 276–283, Apr. 2015.

[12] S. Kondo, T. Hinoki, M. Nonaka, and K. Ozawa, “Irradiation-induced shrinkage of highly crystalline SiC fibers,” *Acta Mater.*, vol. 83, pp. 1–9, Jan. 2015.

[13] T. Koyanagi, T. Nozawa, Y. Katoh, and L. L. Snead, “Mechanical property degradation of high crystalline SiC fiber–reinforced SiC matrix composite neutron irradiated to ∼100 displacements per atom,” *J. Eur. Ceram. Soc.*, vol. 38, no. 4, pp. 1087–1094, Apr. 2018.

[14] M. Li, “Moving from Dpa to Changes in Materials Properties,” 2012.

[15] S. Plimpton, “Fast Parallel Algorithms for Short-Range Molecular Dynamics,” *J. Comput. Phys.*, vol. 117, no. 1, pp. 1–19, Mar. 1995.

[16] L. A. Zepeda-Ruiz, A. Stukowski, T. Oppelstrup, and V. V. Bulatov, “Probing the limits of metal plasticity with molecular dynamics simulations,” *Nature*, vol. 550, no. 7677, pp. 492–495, Oct. 2017.

[17] T. A. HUNT and B. D. TODD, “On the Arnold cat map and periodic boundary conditions for planar elongational flow,” *Mol. Phys.*, vol. 101, no. 23–24, pp. 3445–3454, Dec. 2003.

[18] J. P. Mithen, “Molecular dynamics simulations of the equilibrium dynamics of non-ideal plasmas,” 2012.

[19] M. S. Daw and M. I. Baskes, “Embedded-atom method: Derivation and application to impurities, surfaces, and other defects in metals,” *Phys. Rev. B*, vol. 29, no. 12, pp. 6443–6453, Jun. 1984.

[20] J. Tersoff, “New empirical model for the structural properties of silicon,” *Phys. Rev. Lett.*, vol. 56, no. 6, pp. 632–635, Feb. 1986.

[21] J. Tersoff, “Modeling solid-state chemistry: Interatomic potentials for

multicomponent systems," *Phys. Rev. B*, vol. 39, no. 8, pp. 5566–5568, Mar. 1989.

[22] P. Erhart and K. Albe, "Analytical potential for atomistic simulations of silicon, carbon, and silicon carbide," *Phys. Rev. B*, vol. 71, no. 3, p. 035211, Jan. 2005.

[23] P. F. Zou, R. F. W. Bader, and IUCr, "A topological definition of a Wigner–Seitz cell and the atomic scattering factor," *Acta Crystallogr. Sect. A Found. Crystallogr.*, vol. 50, no. 6, pp. 714–725, Nov. 1994.

[24] G. D. Samolyuk, Y. N. Osetsky, and R. E. Stoller, "Molecular dynamics modeling of atomic displacement cascades in 3C–SiC: Comparison of interatomic potentials," *J. Nucl. Mater.*, vol. 465, pp. 83–88, Oct. 2015.

[25] K. Vörtler, "Computer simulation of multi-elemental fusion reactor materials." 2011.

[26] R. Behrisch and W. Eckstein, *Sputtering by particle bombardment : experiments and computer calculations from threshold to MeV energies*. Springer, 2007.

[27] G. Lucas and L. Pizzagalli, "Ab initio molecular dynamics calculations of threshold displacement energies in silicon carbide," Sep. 2007.

[28] I. A. Hønstvet, R. E. Smallman, and P. M. Marquis, "A determination of the atomic displacement energy in cubic silicon carbide," *Philos. Mag. A*, vol. 41, no. 2, pp. 201–207, Feb. 1980.

[29] S. J. Zinkle and C. Kinoshita, "Defect production in ceramics," *J. Nucl. Mater.*, vol. 251, pp. 200–217, Nov. 1997.

[30] H. Huang, N. M. Ghoniem, J. K. Wong, and M. Baskes, "Molecular dynamics determination of defect energetics in beta -SiC using three representative empirical potentials," *Model. Simul. Mater. Sci. Eng.*, vol. 3, no. 5, pp. 615–627, Sep. 1995.

[31] M. I. Norgett, M. T. Robinson, and I. M. Torrens, "A PROPOSED METHOD OF CALCULATING DISPLACEMENT DOSE RATES."

[32] M. T. Robinson, "Basic physics of radiation damage production," *J. Nucl. Mater.*, vol. 216, pp. 1–28, Oct. 1994.

[33] J. Lindhard, "This Week's Citation Classic," 1963.

[34] J. R. Beeler, *Radiation effects, computer experiments*. North-Holland Pub. Co.,

1983.

[35] D. E. Farrell, *Vacancy clustering phenomena in silicon carbide reactor components : a multiple time-scale atomistic problem.* .

[36] S. Fujita, J. R. Mcnabb Iii, H.-C. Ho, and A. Suzuki, "Lattice Stability and Reflection Symmetry," *J. Mod. Phys.*, vol. 6, pp. 691–697, 2015.

[37] Frank Zirkelbach, "Atomistic simulation study on silicon carbide precipitation in silicon," Universit¨at Augsburg, 2012.

[38] C. D. Latham, A. J. McKenna, T. P. Trevethan, M. I. Heggie, M. J. Rayson, and P. R. Briddon, "On the validity of empirical potentials for simulating radiation damage in graphite: a benchmark," *J. Phys. Condens. Matter*, vol. 27, no. 31, p. 316301, Aug. 2015.

[39] M. Bockstedte, A. Mattausch, and O. Pankratov, "*Ab initio* study of the annealing of vacancies and interstitials in cubic SiC: Vacancy-interstitial recombination and aggregation of carbon interstitials," *Phys. Rev. B*, vol. 69, no. 23, p. 235202, Jun. 2004.

[40] X. K. Lu, T. Y. Xin, Q. Zhang, Y. J. Feng, X. L. Ren, and Y. X. Wang, "Decentral distribution of helium in β-SiC: Studied by density functional theory," *Nucl. Mater. Energy*, vol. 13, pp. 35–41, Dec. 2017.

[41] G. Lucas and L. Pizzagalli, "Structure and stability of irradiation-induced Frenkel pairs in 3C-SiC using first principles calculations," *Nucl. Instruments Methods Phys. Res. Sect. B Beam Interact. with Mater. Atoms*, vol. 255, no. 1, pp. 124–129, Feb. 2007.

[42] E. J. Bylaska, K. Tsemekhman, and F. Gao, "New development of self-interaction corrected DFT for extended systems applied to the calculation of native defects in 3C–SiC," *Phys. Scr.*, vol. T124, no. T124, pp. 86–90, May 2006.

[43] A. A. El-Barbary, R. H. Telling, C. P. Ewels, M. I. Heggie, and P. R. Briddon, "Structure and energetics of the vacancy in graphite," *Phys. Rev. B*, vol. 68, no. 14, p. 144107, Oct. 2003.

[44] L. Li, S. Reich, and J. Robertson, "Defect energies of graphite: Density-functional

calculations."

[45] J. P. Perdew and Y. Wang, "Accurate and simple analytic representation of the electron-gas correlation energy," *Phys. Rev. B*, vol. 45, no. 23, pp. 13244–13249, Jun. 1992.

[46] J. P. Perdew, K. Burke, and M. Ernzerhof, "Generalized Gradient Approximation Made Simple," *Phys. Rev. Lett.*, vol. 77, no. 18, pp. 3865–3868, Oct. 1996.

[47] R. Devanathan, T. Diaz de la Rubia, and W. J. Weber, "Displacement threshold energies in β-SiC," *J. Nucl. Mater.*, vol. 253, no. 1–3, pp. 47–52, Mar. 1998.

[48] R. Rurali, E. Hernández, P. Godignon, J. Rebollo, and P. Ordejón, "First-principles studies of the diffusion of B impurities and vacancies in SiC," *Phys. Rev. B*, vol. 69, no. 12, p. 125203, Mar. 2004.

[49] F. Gao, R. Devanathan, and W. J. Weber, "Si Displacement Cascades Revealed by Atomic-Scale Simulations in 3C-SiC," *Fusion Technol.*, vol. 39, no. 2P2, pp. 574–578, Mar. 2001.

[50] A. Misra and L. Thilly, "Structural metals at extremes," *MRS Bull.*, vol. 35, no. 12, pp. 965–977, 2010.

[51] S. Stankovich *et al.*, "Graphene-based composite materials," *Nature*, vol. 442, no. 7100, pp. 282–286, Jul. 2006.

[52] T. Kuilla, S. Bhadra, D. Yao, N. H. Kim, S. Bose, and J. H. Lee, "Recent advances in graphene based polymer composites," *Prog. Polym. Sci.*, vol. 35, no. 11, pp. 1350–1375, Nov. 2010.

[53] M. Li, J. Zhang, X. Hu, and Y. Yue, "Thermal transport across graphene/SiC interface: effects of atomic bond and crystallinity of substrate," *Appl. Phys. A*, vol. 119, no. 2, pp. 415–424, May 2015.

[54] M. Inoue, H. Kageshima, Y. Kangawa, and K. Kakimoto, "First-principles calculation of 0 th -layer graphene-like growth of C on SiC(0001)," *Phys. Rev. B*, vol. 86, no. 8, p. 085417, Aug. 2012.

[55] N. Swaminathan, M. Wojdyr, D. D. Morgan, and I. Szlufarska, "Radiation interaction with tilt grain boundaries in β-SiC," *J. Appl. Phys.*, vol. 111, no. 5, p.

054918, Mar. 2012.

[56] O. J. Guy and K.-A. D. Walker, “Graphene Functionalization for Biosensor Applications,” *Silicon Carbide Biotechnol.*, pp. 85–141, Jan. 2016.

[57] B. Gupta, E. Placidi, C. Hogan, N. Mishra, F. Iacopi, and N. Motta, “The transition from 3C SiC(111) to graphene captured by Ultra High Vacuum Scanning Tunneling Microscopy,” *Carbon N. Y.*, vol. 91, pp. 378–385, Sep. 2015.

[58] N. Mishra, J. Boeckl, N. Motta, and F. Iacopi, “Graphene growth on silicon carbide: A review,” *Phys. status solidi*, vol. 213, no. 9, pp. 2277–2289, Sep. 2016.